Lithos 248–251 (2016) 339–352

Contents lists available at ScienceDirect

Lithos

journal homepage: www.elsevier.com/locate/lithos

Asthenosphere–lithosphere interactions in Western Saudi Arabia: Inferences from $^{3}He/^{4}He$ in xenoliths and lava flows from Harrat Hutaymah

Kevin Konrad [a,*], David W. Graham [a], Carl R. Thornber [b], Robert A. Duncan [a], Adam J.R. Kent [a], Abdullah M. Al-Amri [c]

[a] College of Earth, Ocean, and Atmospheric Sciences, Oregon State University, Corvallis, OR 97331-5503 USA
[b] U.S. Geological Survey, Cascades Volcano Observatory, Vancouver, WA, USA
[c] Department of Geology and Geophysics, King Saud University, Riyadh, Saudi Arabia

ARTICLE INFO

Article history:
Received 23 October 2015
Accepted 30 January 2016
Available online 10 February 2016

Keywords:
Arabia
Harrat volcanism
Lithosphere–asthenosphere boundary
SCLM
Noble gases
Helium isotopes

ABSTRACT

Extensive volcanic fields on the western Arabian Plate have erupted intermittently over the last 30 Ma following emplacement of the Afar flood basalts in Ethiopia. In an effort to better understand the origin of this volcanism in western Saudi Arabia, we analyzed $^{3}He/^{4}He$, and He, CO_2 and trace element concentrations in minerals separated from xenoliths and lava flows from Harrat Hutaymah, supplemented with reconnaissance He isotope data from several other volcanic fields (Harrat Al Birk, Harrat Al Kishb and Harrat Ithnayn). Harrat Hutaymah is young (<850 ka) and the northeasternmost of the volcanic fields. There is a remarkable homogeneity of $^{3}He/^{4}He$ trapped within most xenoliths, with a weighted mean of 7.54 ± 0.03 R_A (2σ, $n = 20$). This homogeneity occurs over at least eight different xenolith types (including spinel lherzolite, amphibole clinopyroxenite, olivine websterite, clinopyroxenite and garnet websterite), and encompasses ten different volcanic centers within an area of ~2500 km^2. The homogeneity is caused by volatile equilibration between the xenoliths and fluids derived from their host magma, as fluid inclusions are annealed during the infiltration of vapor-saturated magmas along crystalline grain boundaries. The notable exceptions are the anhydrous spinel lherzolites, which have a lower weighted mean $^{3}He/^{4}He$ of 6.8 ± 0.3 R_A (2σ, $n = 2$), contain lower concentrations of trapped He, and have a distinctly depleted light rare earth element signature. $^{3}He/^{4}He$ values of ~6.8 R_A are also commonly found in spinel lherzolites from harrats Ithnayn, Al Birk, and from Zabargad Island in the Red Sea. Olivine from non-xenolith-bearing lava flows at Hutaymah spans the He isotope range of the xenoliths. The lower $^{3}He/^{4}He$ in the anhydrous spinel lherzolites appears to be tied to remnant Proterozoic lithosphere prior to metasomatic fluid overprinting. Elevated $^{3}He/^{4}He$ in the western harrats has been observed only at Rahat (up to 11.8 R_A; Murcia et al., 2013), a volcanic field situated above thinned lithosphere beneath the Makkah-Medinah-Nafud volcanic lineament. Previous work established that spinel lherzolites at Hutaymah are sourced near the lithosphere-asthenosphere boundary (LAB), while other xenolith types there are derived from shallower depths within the lithosphere itself (Thornber, 1992). Helium isotopes are consistent with melts originating near the LAB beneath many of the Arabian harrats, and any magma derived from the Afar mantle plume currently appears to be of minor importance.

1. Introduction

Numerous volcanic fields (harrats) occur in the western half of the Arabian plate, from Yemen in the south to Syria in the north. The origin of this continental volcanism remains enigmatic. The oldest fields are ~30 Ma in Yemen and are associated with the earliest volcanism produced by the Afar mantle plume and eruption of flood basalts in Ethiopia and Yemen (Stern and Johnson, 2010). The onset of harrat volcanism is roughly synchronous with opening of the Red Sea and uplift of the Arabian shield (Bohannon et al., 1989). There appears to be a rough age progression from 15 to 30 Ma in southwestern Arabia to presently active volcanism in northwestern Saudi Arabia (Coleman et al., 1983). In contrast, the corresponding area of the African plate on the western margin of the Red Sea has not seen uplift or volcanism of a similar magnitude.

One model for the source of harrat volcanism is entrainment and melting of Afar mantle plume material beneath western Saudi Arabia. An anomalous channel of low seismic velocity exists in the upper mantle beneath this region that has been interpreted as flow of a mantle

* Corresponding author.
E-mail address: konradke@geo.oregonstate.edu (K. Konrad).

http://dx.doi.org/10.1016/j.lithos.2016.01.031
0024-4937/

plume northward from beneath the Afar triple junction (Chang and Van der Lee, 2011). A quasi-vertical anomaly also exists beneath Jordan and northern Arabia, possibly representing a separate plume responsible for volcanic fields extending from northern Arabia to southern Turkey.

A second model for the source of harrat volcanism is east-west extensional thinning of the lithosphere and consequent melting of upwelling asthenosphere (Bertrand et al., 2003; Moufti et al., 2012; Shaw et al., 2003). This regional extension results from uplift and tectonic stress driven by the presence of the Afar plume at depth, and leads to formation of lithospheric fractures that act as pathways for magma migration. Slab pull beneath the Aegean coupled with Afar plume upwelling helps to drive a large-scale, anti-clockwise toroidal flow beneath the Arabia–Anatolia–Aegean region (Faccenna et al., 2013). Harrat magmatism may also be linked to Red Sea extension, but its exact relation to Afro-Arabian rifting remains unclear (e.g. Camp and Roobol, 1992; Hempton, 1987). A third proposed model for the source of harrat volcanism is reactivation of "fossilized" plume material at the base of the lithosphere (e.g., Stein and Hofmann, 1992), potentially triggered by thinning or extension of the lithosphere (Altherr et al., 1990).

Helium isotopes are one of the best indicators of a deep mantle plume source, and the Afar plume is characterized by elevated $^3He/^4He$. Numerous basalts in the Main Ethiopian Rift, Southern East African Rift and Afar region have $^3He/^4He$ ratios above 10 R_A, where R_A is the atmospheric ratio of 1.39×10^{-6} (Barry et al., 2013; Hilton et al., 2011; Darrah et al., 2012; Halldorsson et al., 2014; Marty et al., 1996; Pik et al., 2006; Rooney et al., 2012; Scarsi and Craig, 1996). These ratios are significantly higher than values of 6 to 10 R_A typically found in mid-ocean ridge basalts derived from the upper mantle (Graham, 2002). The highest $^3He/^4He$ found in the Afar region to date is ~21 R_A, in the Oligocene flood basalts of Ethiopia associated with very early stages of plume volcanism (Stuart, 2013). If Afar plume material extends beneath the Arabian Plate and provides a mantle source component for volcanism, then elevated $^3He/^4He$ should be found in the western harrats.

Helium isotope data on young basalts (<10 ka) comprising Harrat Rahat provide the strongest indication of an Afar plume influence on harrat volcanism. These alkaline olivine-phryic basalts have $^3He/^4He$ values of 9.3–11.8 R_A, suggesting a weak but detectable plume helium signal (Murcia et al., 2013). In contrast, $^3He/^4He$ data for both metasomatically altered and unaltered mantle xenoliths from the Al Kishb and Jizan volcanic fields of Saudi Arabia, and from Bir Ali in Yemen range between 6 and 8 R_A, typical of lithospheric and asthenospheric sources (Hopp et al., 2004; Sgualdo et al. 2015). Volcanic activity in western Saudi Arabia and Yemen thus appears to access asthenosphere, plume and lithospheric components, and their relative contributions may be related to a range of tectonic factors such as setting with respect to the rift axis (on-rift vs. off-rift), duration of magmatism and degree of lithospheric involvement.

The harrats throughout western Saudi Arabia contain diverse suites of xenoliths, providing a window into the crust and lithospheric mantle beneath the region. Helium isotope variations in ultramafic xenoliths are useful for distinguishing the effects of metasomatic fluids derived from the crust vs. the mantle (e.g., Barry et al., 2015). Ultramafic xenoliths often display a "decoupling" between volatile elements such as He and lithophile elements such as Sr (e.g. Dunai and Porcelli, 2002). A common explanation for this decoupling is an open-system exchange between the lithosphere and asthenosphere that involves preferential volatile transport from the upper mantle into the lithosphere (Bailey, 1982; Wass and Rogers, 1980). This metasomatism is a process whereby lithospheric mantle becomes enriched in CO_2 and He, thereby overwhelming prior lithospheric He isotope signatures while having little, if any, effect on the intrinsic signatures of lithophile elements (Hilton and Porcelli, 2003). Consequently, $^3He/^4He$ ratios of deep crustal and mantle xenoliths associated with recent continental volcanism often show an asthenospheric signature (Day et al., 2015). Their $^3He/^4He$ resemble those of host lavas or uppermost asthenosphere rather than low $^3He/^4He$ ratios that would be produced by long-term ^4He ingrowth within the lithosphere or crust.

In this study we report He, CO_2, and trace element concentrations, and He isotope ratios from 18 different xenoliths and four lava flows from Harrat Hutaymah (n = 26, including multiple phases of the same rock). The results provide a test of the presence of Afar plume material in this distal region of harrat volcanism. They also provide a detailed picture of He isotope variability of the sub-continental lithospheric mantle (SCLM) within a relatively small region (~2500 km^2) of harrat volcanism, as well as the extent to which He isotopes and He/CO_2 ratios are effective tracers of mantle metasomatism. Collectively the He isotope and trace element results provide information on the origin of alkali basaltic volcanism throughout western Saudi Arabia and the involvement of a young plume vs. ancient lithosphere in magma genesis.

2. Regional background

The distribution, structure and timing of the volcanic fields of western Arabia, summarized in Camp and Roobol (1992), show evidence for distinct phases of magmatism. The earlier phase occurred between ~30 and 20 Ma and produced tholeiitic (quartz-normative) to transitional (nepheline-normative and hypersthene-normative) basalt along northwest trends, and is attributed to passive mantle upwelling during extension of the Red Sea (Camp and Roobol, 1992). The later phase occurred between ~12 Ma and the present, and produced transitional to strongly-alkalic lava erupted from centers aligned along north–south trends that form the harrats. Collectively, the Arabian harrats comprise one of the largest alkali basalt provinces in the world with an area of ~180,000 km^2.

The Cenozoic harrats lie unconformably on Precambrian crystalline rocks (the Arabian Shield) and Phanerozoic sedimentary sequences that comprise much of the Arabian Plate. Most of the shield rocks are Neoproterozoic in age (540–1000 Ma) but locally there are outcrops of older basement ranging to Archean (Stein, 2003; Stern and Johnson, 2010). The eastern sector of the shield appears to have a different history that may relate to the presence of a lithospheric boundary marking the former collision zone between east and west Gondwana (Stoeser and Frost, 2006). Lead and Nd isotopes from Arabian shield granitoid rocks delineate the involvement of distinct eastern and western arc terranes in the history of the crust and lithospheric mantle. Furthermore, the eastern shield group is marked by higher $^{208}Pb/^{206}Pb$ and positive initial ε_{Nd} compositions indicating ancient oceanic mantle, potentially mixed with cratonic material, as a magma source during the late Precambrian (Stoeser and Frost, 2006). Pre-existing mantle heterogeneity is likely to have been significant, through tectonic convergence/accretion of oceanic plateaus (e.g. Stern and Johnson, 2010) and/or the trapping of "fossilized" plume mantle beneath the lithosphere (Stein, 2003; Stein and Hofmann, 1992).

Bulk-rock trace element data for harrat basalts suggest that magma generation occurs near the lithosphere–asthenosphere boundary (LAB) (e.g. Bertrand et al., 2003; Duncan and Al-Amri, 2013; Shaw et al., 2003) or within the lithosphere itself (Thornber, 1992; Thornber, 1994). Pb isotopic data for Arabian harrats indicate the presence of a 'high-μ' signature (an enriched $^{206}Pb/^{204}Pb$ ratio produced by a long-lived reservoir having a high U/Pb ratio) that may be interpreted either as a plume-related component (Krienitz et al., 2009) or related to melting of ancient lithospheric metasomes (Bertrand et al., 2003; Rooney et al., 2014).

2.1. Significance of Harrat Hutaymah

Harrat Hutaymah is an alkali basalt volcanic field in north central Arabia covering an area of ~2500 km^2 (Fig. 1). The harrat is unique in that it skirts the boundary between western and eastern Arabia, which record differences in accretion history (Stoeser and Frost, 2006). All recent $^{40}Ar/^{39}Ar$ age determinations of lava flows at Hutaymah are younger than 850 ka (Duncan et al., 2016). The volcanic field lies at the northeastern boundary of the Arabian Shield and is the most eastward

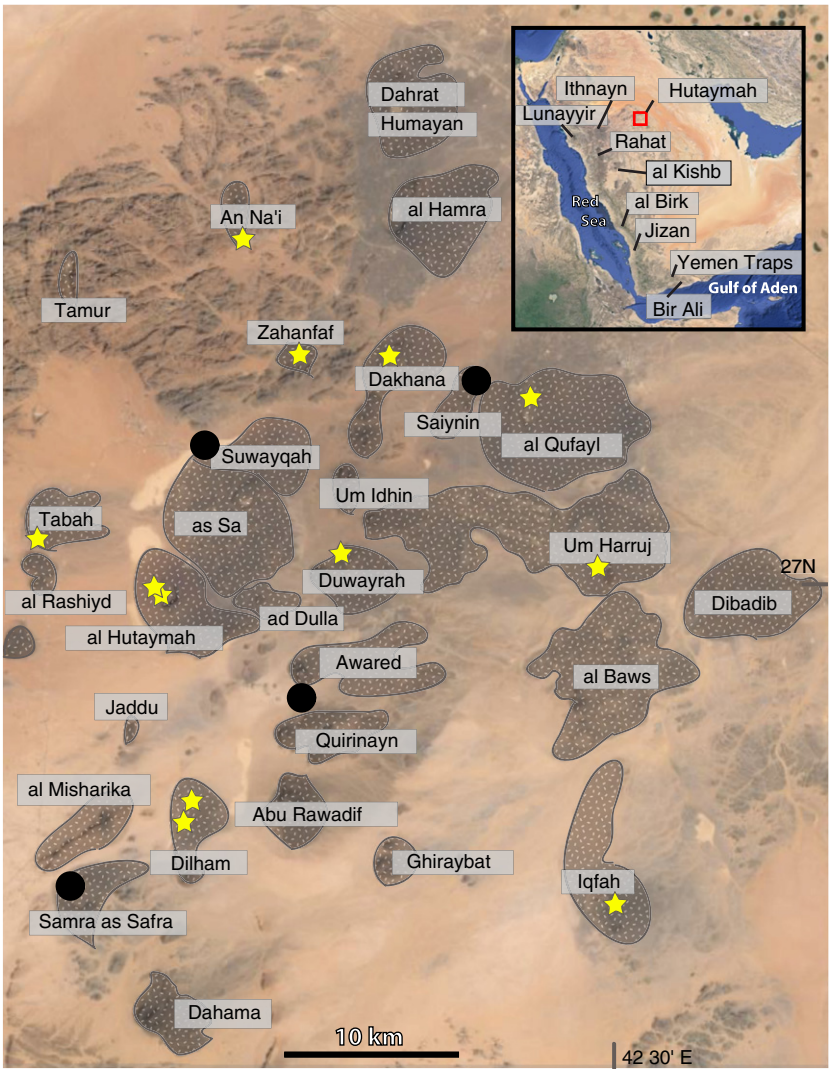

Fig. 1. Modified satellite image of Harrat Hutaymah. Inset shows a regional map of Saudi Arabia with some major harrats and features noted. The location of Harrat Hutaymah is highlighted with a red box in the inset. Volcanic centers and fields are highlighted with corresponding names according to Thornber (1990). Yellow stars show locations of xenoliths analyzed in this study and black circles show analyzed basalts.

extent of harrat volcanism, some 500 km from the Red Sea (Coleman et al., 1983; Pallister, 1984). Hutaymah is one of the smallest Arabian harrats, containing the largest proportion of exposed tephra deposits from annular tuff rings in addition to more typical cinder and spatter cones with effusive lava flows (Thornber, 1990). The prevalence of mantle xenolith-bearing tuff suggests CO_2-charged basanite diatreme volcanism in the region (e.g. Spera, 1984; Wass and Rogers, 1980).

Hutaymah tephra and lava flows contain nearly the full diversity of ultramafic xenolith types that are found globally in association with intraplate, mafic alkaline volcanism. Thornber (1994) divided the xenoliths into chromium-diopside (type I) and aluminous augite lithologies (type II), which may be further subdivided based upon mineralogy and texture into 26 subgroups. The aluminous augite lithologies are believed to have been entrained from within 10 km of the base of the ~40 km thick crust, based on experimental constraints and thermobarometric calculations (Thornber, 1994). Within the chromium-diopside group, the pristine spinel lherzolite xenoliths appear to come from a maximum depth of ~ 70 km. One group of xenoliths falls along a Sm-Nd pseudo-isochron (n = 3) having an age of 700 Ma, suggesting a source within Proterozoic lithosphere (Thornber, 1992). These ages are similar to Sm-Nd ages of ~600–800 Ma determined from other Arabian xenoliths (Bertrand et al., 2003; Blusztajn et al., 1995; Henjes-Kunst et al., 1990; Krienitz and Haase, 2011; Stein and Hofmann, 1992; Stern and Johnson, 2010). Notably, however, Lu-Hf model ages for Arabian and Yemen xenoliths are typically late Proterozoic (1.5–2 Ga) (e.g. Sgualdo et al., 2015; Shaw et al., 2007). These older model ages may be more reliable due to a lower degree of overprinting in the Lu-Hf system relative to Sm-Nd (e.g. Bedini et al., 2004) and the leaky nature of the Sm-Nd chronometer at mantle temperatures (Albarède, 2003). A second group of Hutaymah xenoliths is considerably younger, presumably reflecting magmatic processes that occurred just prior to or during Quaternary volcanism (Thornber, 1992). The rare earth element (REE) patterns displayed by Hutaymah basalts can be produced by 1–7% partial melting of spinel lherzolite either within the lithosphere (Thornber, 1992) or from an enriched asthenospheric source (Duncan et al., 2016). Trace element patterns in the basalts along with thermobarometric constraints from the xenoliths led Thornber (1992) to postulate that Hutaymah magmas originate within the lithosphere close to the lithosphere-asthenosphere boundary (LAB).

3. Materials and methods

3.1. Samples

Harrat Hutaymah ultramafic xenoliths, along with polished thin sections and mineral separates, were selected for this study from an

extensive and thoroughly analyzed collection reported by Thornber (1990, 1992, 1994). We adopted the group terminology of Thornber (1992) and divide our selected xenoliths into three groups. These include type I (chromium-diopside bearing xenoliths) and type II (aluminous-augite bearing xenoliths). For type II lithologies we report data for four metamorphic xenoliths, but no igneous xenoliths (as described in Thornber, 1992) were analyzed. The metamorphic type II xenoliths are considered to represent Proterozoic deep crust based upon petrology, REEs and isotope compositions (Henjes-Kunst et al., 1990; McGuire and Stern, 1993; Thornber, 1992). A third and notably distinct subgroup within type I is referred to here as code 0 xenoliths. These are chromium-diopside bearing protogranular spinel lherzolites that lack petrographic evidence of fluid metasomatism (e.g. hydrous mineral phases, partial melt, linear fluid inclusion bands) commonly seen in the other subgroups (Fig. 2).

The four olivine-phyric basalts analyzed in this study were collected in 2013 and cover a large spatial range of Harrat Hutaymah (black circles, Fig. 1). These lava flows contained no observable xenoliths and the olivine phenocrysts separated for analysis were subhedral-euhedral with minor iddingsite. These phenocrysts are believed to be cognate and not xenocrystic. Geochemical analyses and age determinations for these samples, along with additional Hutaymah basalts, are presented in Duncan et al. (2016).

For the purpose of preliminary exploration and comparison, helium isotopic analyses were carried out on four additional xenoliths from elsewhere in Saudi Arabia previously analyzed for their chemical compositions and Sr-Nd isotopes (Blusztajn et al., 1995). A fifth uncharacterized xenolith from Al Birk was also analyzed for $^3He/^4He$. All these xenoliths are unfoliated, protogranular spinel lherzolites containing no hydrous phases, and would be classified as code 0 according to Thornber (1992). The three Al Kishb xenoliths have depleted REE patterns relative to chondrites, while the Ithnayn xenolith has a flat to LREE-enriched pattern (Blusztajn et al., 1995).

3.2. Helium and CO_2 analyses

We separated minerals from xenoliths and bulk lava by crushing, sieving and magnetic separation. The majority of xenoliths analyzed in this study were already crushed and magnetically separated for analysis in Thornber (1990, 1994). Minerals from size fractions ranging from 212 to 750 μm were hand-picked to be free of surface alteration using a binocular microscope. Samples were ultrasonically cleaned in ethanol for 15 minutes followed by two 15 minute acetone baths with rinsing in between. The final separate was air dried, weighed and loaded into online crushers. Between 200 and 500 mg of sample were loaded for each analysis.

Helium and CO_2 were analyzed by *in vacuo* crushing following methods described by Graham et al. (2014a). Released gases were exposed to a U-trap held at liquid nitrogen temperature (77 K) during the crushing in order to trap the major volatiles of H_2O and CO_2. Non-condensable gases were then passed through the U-trap and exposed to a sequence of SAES (Zr-Al alloy) getters. Exposure for five minutes to the first getter as it cooled from ~400 °C was followed by two minute exposure to a second SAES getter held at room temperature. The noble gases were then adsorbed onto activated charcoal at 10 K using a Janis cryostat. Helium was separated from the other noble gases by release from the cryostat at 45 K, and admitted to a Nu instruments Noblesse mass spectrometer. Following this, the U-trap was isolated, and CO_2 was separated from H_2O by switching to a frozen isopropanol trap (190 K) on the U-trap and distilling the CO_2 using liquid N_2 on a cold finger within a calibrated volume of the sample preparation line. The partial pressure of CO_2 was measured using a high precision capacitance manometer (1 torr full-scale MKS baratron) after the cold finger was warmed to room temperature. For upper mantle-derived melts, as exemplified by MORBs, CO_2 is the dominant volatile phase (>95%; Moore et al., 1977), while in mantle xenoliths it is commonly 80% or more (Burnard et al., 1994). We therefore consider contributions from other volatiles which we cannot distinguish by our methods, such as N_2, CO and CH_4, to be negligible within the uncertainty of our measurements. The stability of the baratron allows for detection of CO_2 concentrations as low as 1×10^{-5} ccSTP. However, in a more conservative effort the CO_2 cut-off limit was placed at 9×10^{-5} ccSTP (1 mtorr).

The mass spectrometer was operated in static mode, utilizing peak switching through control of the magnetic field, in order to measure ^3He, ^4He and HD. The HD peak was monitored during all analyses because ^3He is not fully resolved from HD in the OSU mass spectrometer. However, beneath the peak flat where ^3He is measured the HD count rate is effectively the same as the background away from the ^3He peak, and any contribution from interference by HD was below the

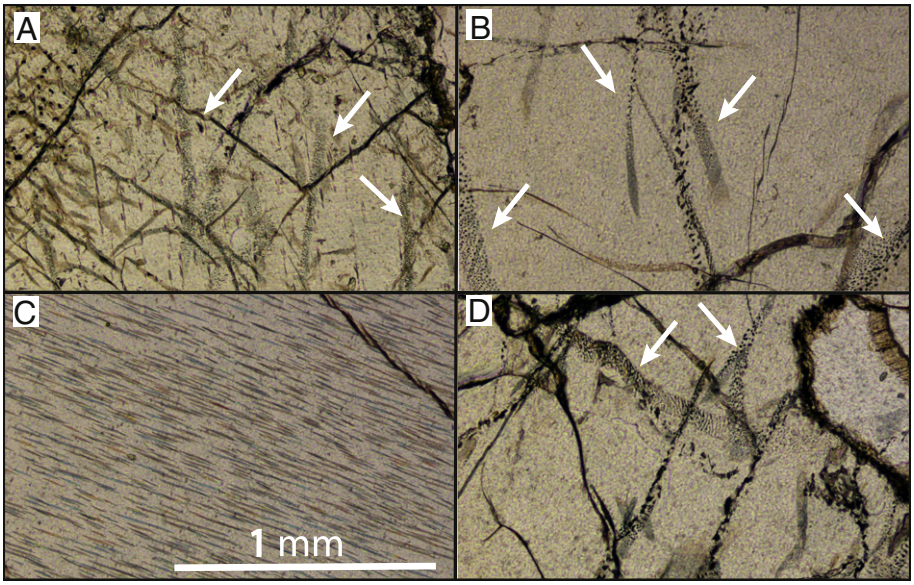

Fig. 2. Plane-polarized-light images of diopside crystals from Hutaymah xenoliths. White arrows indicate the location of fluid inclusion bands. Scale bar of 1 mm applies to all images. A) Diopside from an amphibole-bearing, type I clinopyroxenite (176611B). B) Diopside from a type I olivine-websterite (176709-2). C) Diopside from a code 0 anhydrous spinel-lherzolite (176735A) with finely exsolved orthopyroxene. Note the lack of inclusions and deformation in code 0 samples. D) Augite from a type II garnet-websterite (176696-35).

analytical precision of the analysis (which is primarily controlled by ion counting statistics on the ^{3}He ion beam). Line blanks were run before each sample and the measured ^{3}He and ^{4}He in all samples were blank corrected. Typically blanks were $< 1 \times 10^{-10}$ ccSTP for ^{4}He and $\leq 1 \times 10^{-15}$ ccSTP for ^{3}He. Numerous aliquots of a running standard of HESJ (Helium Standard of Japan; Matsuda et al., 2002) were analyzed throughout this study. The HESJ standard is a split of the same gas used in the helium isotope lab at NOAA/PMEL in Newport, OR. It has a ^{3}He/^{4}He ratio of 20.4 R_A, determined in the OSU lab compared to marine air collected in 2007, in agreement with the value reported by Lupton and Evans (2004). For the majority of samples in this study, the reproducibility of ^{3}He/^{4}He for HESJ standards in the size range of the samples was better than ± 0.5% (1σ). All ^{3}He/^{4}He errors are reported as 2σ and include the analytical uncertainty from ion counting and the reproducibility of the HESJ standard.

3.3. Trace element analyses

Grains of clinopyroxene, orthopyroxene and of a single amphibole were analyzed for the trace elements Li, Ti, Rb, Sr, Y, Zr, Nb, Ba, the rare earth elements (REE), Pb, U, and Th using laser ablation ICP-MS at Oregon State University. Samples were ablated using a Photon Machines Analyte G2 nm ArF "fast" Excimer Laser and elemental concentrations were determined using a Thermo Xseries-2 ICP-MS. Analysis followed general techniques outlined in Loewen and Kent (2012). Samples were ablated using a 30 μm spot size with a laser output of 70% and a fluence of 4.84 J/cm^2. Three grains of each target mineral were analyzed and the values were averaged. Background concentrations were collected for 30 seconds prior to each analysis. Standards were run before, during, and after the batch runs and included the USGS basaltic glass standards GSE-1G, GSD-1G, BHVO-2G, and BCR-2G run as secondary standards, and GSE-1G was run as the calibration standard. Measured concentrations of trace elements in the secondary standards were typically within 5% of the accepted values (see supplementary material). Reported uncertainties for secondary standards and unknowns include contributions from the measurement of normalized ratios in the unknown, the reproducibility of the standard, and uncertainties in the accepted standard concentrations and the internal standard element (see Loewen and Kent, 2012 for more details). When possible, sample concentrations were internally normalized to CaO (reported by Thornber, 1992). For samples without prior major element determinations, CaO of 22 wt % was assumed for diopside and 1 wt % for enstatite. These samples with assumed CaO contents are designated with an asterisk in Table 2.

4. Results

Helium isotope ratios, and He and CO_2 concentrations for Hutaymah xenolith and lava flow phenocryst separates are reported in Table 1. Trace element results determined by laser ablation ICP-MS are reported in Table 2. Additional He and CO_2 results for xenoliths from other Saudi Arabia localities are reported in Table 3. Trace element patterns are consistent with the instrumental neutron activation analysis (INAA) of bulk xenoliths reported in Thornber (1992), with the exception of the LREE depleted grains from samples 176719-8 and 176611B (see discussion below).

4.1. Non-metasomatized spinel lherzolites (code 0)

Two spinel lherzolites showing no petrographic evidence of metasomatic alteration were analyzed for He, CO_2 and trace elements. Chondrite-normalized REE patterns show a general depletion from the heavy to middle REEs, but the two samples diverge in their LREE characteristics. Sample 176735A shows relative enrichment in Nd that increases towards La, producing a trough-shaped pattern (Fig. 3A). Sample 176719-8 shows strong LREE depletion with La and Nd near detection limits. Both of these xenoliths have the same ^{3}He/^{4}He ratio of 6.8 ± 0.3 R_A and a He concentration of ~8 × 10^{-9}ccSTP/g (8 nccSTP/g; Fig. 4). Their CO_2 concentrations were too low to measure with confidence. We note that Thornber (1992) reports that all other spinel lherzolites from the Dakhana tuff ring contained partial melt and that these code 0 samples might also contain partial melt but not in the area of the polished thin section.

4.2. Chromium-diopside xenoliths (type I)

The metasomatized, diopside-bearing xenoliths display roughly homogeneous REE patterns with a slight LREE enrichment (and with La showing a slight depletion relative to other LREEs in most cases, Fig. 3B). An exception is sample 176611B, which contained two grains with significant LREE depletion and one grain with a LREE enrichment similar to all other type I diopsides. The type I xenoliths display a restricted range of ^{3}He/^{4}He, with a weighted mean of 7.56 ± 0.04 R_A (2σ, n = 16). The ^{4}He concentrations vary from 10 to 650 nccSTP/g. The CO_2/^{3}He ratios of the type I samples are also relatively homogeneous with values between 2.1 and 5.4 × 10^9. Four samples (176748-7, 176611B, 176707-27, 176696-16) are exceptions and contained only trace amounts of CO_2 (Fig. 5). There appear to be only minor differences in the He and CO_2 characteristics of orthopyroxene and clinopyroxene separated from the same xenolith in type I samples (Table 1).

4.3. Garnet and spinel aluminous augite pyroxenite xenoliths (type II)

For the type II samples, two separate metamorphic groups were analyzed: one sample of spinel-sapphirine-bearing websterite (176604C) and three of garnet-bearing websterite (176721-1, 197532, and 176696-35). Augite from sample 176604C shows a slight LREE-depleted pattern (Fig. 3C). Augite grains from the garnet-bearing websterites display humped patterns having both LREE and HREE depletions. These three garnet websterites (code 24 of Thornber, 1992) also show the most CO_2 enrichment relative to He, with CO_2/^{3}He ratios between 9 × 10^9 and 2.3 × 10^{10}. It is important to note that the augite separate analyzed for He from sample 176696-35 also contained up to 20% intergrowths of garnet.

4.4. Lava

Olivine phenocrysts from the four basalts contain low concentrations of He and CO_2 relative to the average xenolith. The ^{3}He/^{4}He ranged from 5.8 to 7.8 R_A, with the lowest ratio occurring in the sample having the lowest He concentration. It is commonly observed that low He concentration samples fall below the mean trend due to the increased susceptibility to extraneous or post-eruptive radiogenic ^{4}He on the ^{3}He/^{4}He ratio. Excluding this single low ^{3}He/^{4}He sample, the range of ^{3}He/^{4}He in the other three basalt samples is 7.2–7.8 R_A, identical to that observed in all xenoliths except for the code 0 anhydrous spinel lherzolites. CO_2 concentrations in olivine phenocrysts from the lava samples were below detection limits.

4.5. Xenoliths from other harrats

Olivine from five xenoliths taken from other harrats were also analyzed for ^{3}He/^{4}He (Table 3). Olivine from one Al Birk and one Ithnayn xenolith yielded ^{3}He/^{4}He of 6.8 R_A, with He concentrations of ~8 nccSTP/g, while olivine from the three xenoliths from Al Kishb have ratios of 8.1 to 8.3 R_A and He concentrations between 20 and 60 nccSTP/g (Fig. 6). The CO_2 concentration in all of these xenoliths was at or below the detection limit.

Table 1
Helium and CO_2 results for xenoliths and phenocrysts from Harrat Hutaymah.

Sample	Vent location	Rock type[a]	Phase	$^3He/^4He$ R/R_A	2 σ	$[^4He]$ ncc STP/g[b]	$[^3He]$ fcc STP/g	$[CO_2]$[c] mcc STP/g	$CO_2/^3He \times 10^9$
Type I: Mg-Cr group inclusion xenoliths									
176719-8	Dakhana	Sp-lhz(0)	Diopside	6.83	0.42	8.80	84	dl	–
176735A	Dilham	Sp-lhz(0)	Diopside	6.82	0.40	8.05	76	dl	–
176738-1	Tabah	Sp-lhz(1)	Diopside	7.29	0.27	41.0	415	dl	–
176748-7	An Nai	Sp-lhz(1)	Diopside	7.40	0.29	42.9	442	dl	–
"	"	Sp-lhz(1)	Enstatite	7.35	0.41	9.69	99	dl	–
176682-2	Al Qufayl	Sp-lhz(1)	Diopside	7.68	0.12	307	3279	16.97	5.17
176707-1	Duwayrah	Sp-lhz(2)	Diopside	7.44	0.13	233	2411	11.53	4.78
176719-1	Dakhana	Sp-lhz(2)	Diopside	7.61	0.09	651	6885	32.21	4.68
"	"	Sp-lhz(2)	Enstatite	7.64	0.11	369	3925	21.38	5.45
176707-13	Duwayrah	Sp-lhz(4)	Amphibole	7.73	0.13	269	2896	8.92	3.08
176611B	Dilham	am-cpt(5)	Diopside	7.62	0.19	47.2	500	dl	–
"	"	am-cpt(5)	Enstatite	7.26	0.22	45.0	455	dl	–
176709-2	Al Hutaymah	ol-web(7)	Diopside	7.32	0.14	111	1127	4.99	4.43
176748-1	An Nai	op-cpmeg(9)	Diopside	7.63	0.11	135	1429	6.42	4.49
"	"	op-cpmeg(9)	Enstatite	7.81	0.18	117	1269	2.67	2.10
176738-23	Tabah	ol-op-cpt(10)	Diopside	7.50	0.10	481	5018	21.41	4.27
176707-27	Duwayrah	cpmeg(11)	Diopside	7.16	0.22	26.7	265	dl	–
176696-16	South Umm Harruj	cpmeg(11)	Diopside	7.36	0.34	9.52	97.4	dl	–
Type II: Al-Fe-Ti group inclusion xenoliths									
176604C	Al Hutaymah	sp-web(21)	Augite	7.51	0.28	20.1	210	dl	–
176721-1	Zahanfaf	sp-ga-web(24)	Augite	7.38	0.11	192	1967	45.61	23.19
197532	Iqfah	sp-ga-web(24)	Augite	7.31	0.34	10.5	107	1.15	10.72
176696-35	South Umm Harruj	sp-ga-web(24)	Augite	7.48	0.30	27.2	283	2.56	9.05
Lava Samples									
HH11	Suwayqa	Ol-bas	Olivine	5.75	0.54	2.62	21	dl	–
HH09	Saiynin	Ol-bas	Olivine	7.82	0.32	11.9	130	dl	–
HH05	Awared	Ol-bas	Olivine	7.24	0.51	9.12	92	dl	–
HH03	Samra as Safra	Ol-bas	Olivine	7.40	0.30	40.9	421	dl	–

[a] Rock types are simplified as followed: spinel lherzolites (sp-lherz), olivine-orthopyroxene bearing clinopyroxenites (ol-op-cpt), amphibole bearing clinopyroxenites (am-cpt), olivine websterites (ol-web), othropyroxene bearing clinopyroxene megacrysts (op-cpmeg), spinel websterites (sp-web), spinel-garnet websterites (sp-ga-web), and olivine phyric basalts (ol-bas). The number following the rock type is the xenolith code in Thornber (1992), which provides more detailed rock descriptions.
[b] Cubic-centimeters of gas at standard temperature and pressure per gram of mineral (cc STP/g). n = nano (10^{-9}), f = femto (10^{-15}), m = milli (10^{-3}).
[c] dl (near detection limit) indicates that the released CO_2 registered a pressure below 1 mtorr on the capacitance manometer.

5. Discussion

5.1. Origin of the helium isotopic homogeneity at Harrat Hutaymah

A bimodal distribution of $^3He/^4He$ exists among Hutaymah xenoliths. The two protogranular spinel-lherzolite (code 0) xenoliths yielded $^3He/^4He = 6.8\ R_A$ (n = 2), while all the remaining xenolith types show a relatively homogenous distribution centered on a mean of 7.54 R_A (standard deviation: 0.18; range: 0.66 R_A; n = 20). In order to explain this homogeneity in non-code 0 samples, we discuss three different scenarios that outline the He isotopic ratios as a tracer of (I) Proterozoic lithosphere assembly, (II) open system volatile exchange within the lithospheric mantle during its evolution, or (III) recent overprinting by the host magma or pre-eruptive metasomatism. It is possible that more than one of these processes may have affected the measured $^3He/^4He$.

Construction of the sub-continental lithospheric mantle (SCLM) beneath Arabia occurred primarily either during the late stages of the Pan-African orogeny (based on Sm-Nd model ages that assume an initial asthenospheric mantle source; Blusztajn et al., 1995; McGuire and Stern, 1993; Stern and Johnson, 2010; Thornber, 1992), or during late Proterozoic time (based on Lu-Hf model ages; Sgualdo et al., 2015; Shaw et al., 2007). In either of these cases, lithospheric accretion is likely to have led to domains that originated with a range of $^3He/^4He$. Assuming a closed system evolution for ~600 Ma, initial $^3He/^4He$ between 8 and 60 R_A, initial U contents of 1–100 ppb, and Th/U ratios of 2.5 to 3.5, the present day $^3He/^4He$ measured for clinopyroxene should be much less than 1 R_A. Given the range in measured values of U and Th in these xenoliths (ranging up to 150 and 370 ppb respectively; Table 2), highly variable $^3He/^4He$ would be measured today if this was the only process involved. It is clear that the Arabian xenoliths do not approximate a closed system evolution for $^3He/^4He$ over the lifetime of the SCLM.

Diffusive exchange of helium over the lifetime of the lithosphere would help to homogenize $^3He/^4He$ between some xenolith types, but it cannot account for the observed homogeneity over the full range of lithologic types in the Hutaymah suite. The type II augite-bearing pyroxenites have similar $^3He/^4He$ to the type I diopside bearing xenoliths. If diffusive exchange between different mantle domains comprised of these lithologies accounted for their similarity, it would require the exchange to occur over length scales of ~35 to 70 km depth based on petrologic constraints (Thornber, 1994). Hart et al. (2008), using a He diffusion coefficient of 10^{-10} m^2/s, estimate that ^4He concentrations might be modified over ~7 to 16 km length scales in ~1.5 Gyr (e.g., Proterozoic lithosphere). This length scale is too short to account for the $^3He/^4He$ homogeneity observed in the large range of xenolith types analyzed in this study. In addition, although grain boundary diffusion at low temperatures has been shown to enhance helium transport in olivine, the diffusivity of helium at mantle temperatures is similar for helium sited at crystal interfaces and hosted within the lattice (Burnard et al., 2015), indicating that the uniform $^3He/^4He$ of the diopside-bearing type I xenoliths and all the type II xenoliths does not result from large-scale diffusive exchange.

The recent overprinting of an inherited lithospheric $^3He/^4He$, is the most plausible explanation for the predominance of $^3He/^4He$ homogeneity among various xenolith types. This overprint occurred either through infiltration by Tertiary-Quaternary host magmas, or by pre-eruptive metasomatism (likely basaltic fluids; e.g. Barry et al., 2015) in the shallow mantle and deep crust. In addition, three of the four basalts have $^3He/^4He$ within the range of the metasomatized xenolith suite. The Hutaymah basalts analyzed for $^3He/^4He$ in this study are non-xenolith bearing and may have experienced some storage and associated

Table 2
Trace element results for Harrat Hutaymah samples determined by LA-ICPMS analysis. All concentrations are in μg/g.

Sample	176719-8*	176735A	176738-1*	176748-7*	176682-2*	176707-1*	176719-1	176707-13	176738-23	176611B[1]	176611B[2]	176709-2*	176748-1*	176604C	176721-1	197532	176696-35
Phase	Diopside	Diopside	Diopside	Diopside	Diopside	Diopside	Diopside	Amphibole	Diopside	Diopside	Diopside	Diopside	Diopside	Augite	Augite	Augite	Augite
Li	0.94	1.08	1.06	0.48	1.54	1.57	1.88	1.00	1.99	0.86	0.95	1.32	1.73	2.67	3.61	2.02	
Ti	780	964.05	942	2523	3833	8100	1475	19188	3988	1605	1527	4719	2406	4387	7222	4367	4611
Cu	1.32	1.10	2.08	1.26	0.84	2.15	4.12	0.93	8.42	1.32	1.32	3.73	1.60	5.07	4.66	21.71	0.55
Rb			0.04					9.91	0.23							0.12	
Sr	0.15	15.4	577.8	126.1	148.2	123.0	174.3	590.1	59.1	2.9	102.8	61.3	34.0	32.2	60.5	28.7	27.4
Y	9.29	11.75	17.57	13.92	13.50	18.52	11.84	17.70	8.39	13.61	9.22	10.24	12.58	20.08	5.66	4.89	7.44
Zr	0.25	1.52	39.85	32.82	35.05	56.03	40.68	119.55	18.89	1.81	15.79	19.10	12.95	19.37	21.98	15.59	17.09
Nb	0.06	0.04	0.77	0.32	0.82	1.60	1.51	71.44	0.61		0.26	0.41	0.42	0.24	0.29	0.14	0.11
Ba	0.02	0.04	1.00	0.06	0.49	0.14	0.58	288.66	0.33	0.10	0.11	0.09	0.11	0.44	0.05	0.11	0.03
La	0.03	2.03	21.62	6.42	3.07	5.36	8.36	14.03	1.74		5.28	1.55	0.70	0.51	1.45	0.41	0.38
Ce		2.49	85.53	16.82	14.58	20.97	32.77	43.96	7.06	0.05	14.09	6.46	1.97	4.02	7.64	2.13	2.19
Pr		0.20	9.68	1.98	2.45	3.05	3.45	5.50	0.98	0.04	1.53	1.06	0.38	0.70	1.40	0.41	0.57
Nd	0.07	0.59	37.08	7.61	13.47	15.25	13.03	24.43	4.87	0.60	6.40	5.54	2.57	4.59	8.18	3.43	4.23
Sm	0.28	0.33	7.01	1.68	3.34	4.13	2.10	5.65	1.54	0.65	1.32	2.13	1.07	2.18	2.81	1.71	1.74
Eu	0.12	0.19	2.31	0.62	1.30	1.42	0.74	1.95	0.60	0.34	0.49	0.73	0.53	0.90	1.09	0.67	0.81
Gd	0.91	0.74	6.13	1.92	4.01	4.43	2.03	4.90	1.84	1.52	1.30	2.34	2.01	3.17	2.68	1.85	3.07
Tb	0.16	0.18	0.67	0.29	0.46	0.63	0.33	0.63	0.24	0.27	0.27	0.33	0.32	0.55	0.36	0.31	0.38
Dy	1.52	1.76	3.93	2.31	2.97	4.17	2.08	3.82	1.83	2.22	1.97	2.06	2.52	3.88	1.70	1.46	2.25
Ho	0.36	0.43	0.70	0.50	0.51	0.72	0.42	0.61	0.33	0.49	0.35	0.41	0.53	0.76	0.24	0.20	0.33
Er	1.30	1.57	1.96	1.87	1.47	2.42	1.36	2.15	0.99	1.91	1.14	1.31	1.72	2.50	0.63	0.41	0.69
Tm	0.16	0.18	0.22	0.25	0.17	0.22	0.17	0.18	0.11	0.21	0.17	0.11	0.17	0.28	0.04	0.03	0.05
Yb	1.21	1.23	1.42	1.40	0.98	1.29	1.17	1.34	0.72	1.44	1.14	0.82	1.36	2.06	0.20	0.21	0.28
Lu	0.18	0.20	0.16	0.22	0.13	0.16	0.18	0.19	0.09	0.20	0.14	0.09	0.17	0.27	0.02	0.03	
Pb	0.02	0.11	0.38	0.27	0.03	0.05	0.05	0.29	0.03	0.01	0.35	0.01	0.01	0.44	0.35	0.17	0.06
Th		0.35	0.62	0.21	0.05	0.10	0.21	0.45	0.06		0.57	0.04	0.05		0.04	0.02	0.01
U		0.09	0.23	0.05	0.01	0.03	0.05	0.09	0.02		0.18	0.01	0.01		0.03	0.01	
N**	2	3	3	3	3	3	3	2	3	2	1	3	3	3	3	1	2

* Indicate that the concentrations are normalized to an assumed diopside CaO weight percent of 22.
** N(grains) refers to the number of grains analyzed for trace elements. Where different grains gave highly widely variable results for an element, that element may have been excluded. Blank values indicate the concentration in that sample was below detection limit.
[1] Grains from sample 176611B showing depleted trace element characteristics.
[2] A single grain from sample 176611B showing trace element enrichment similar to other type I samples.

Table 3
Helium analysis for olivine separated from spinel lherzolites originally described in Blusztajn et al. (1995).

Sample	Location	$^3He/^4He$ R/R_A	2 σ	[^{4}He] ncc STP/g	[^{3}He] fcc STP/g
H-30-B1	Al Kishb	8.11	0.25	19	209
H-271-1	Al Kishb	8.25	0.22	20	226
H-271-15	Al Kishb	8.29	0.15	59	683
H-132-7	Ithnayn	6.81	0.33	8	75
II-26-D	Al Birk	6.76	0.30	8	79

CO_2 concentrations were at the detection limit and so are not reported for these samples. Units are the same as Table 1.

degassing within crustal magma lenses. This would lead to lower He and CO_2 contents trapped within olivine phenocrysts for the basalts compared to xenolith minerals. In general, olivine phenocrysts in the lava samples also have lower He contents than many of the xenolith minerals (particularly most of the type I group), but they do overlap with the type II xenoliths and the anhydrous spinel lherzolites (code 0 of type I) (Fig. 4). We interpret this overlapping range of $^3He/^4He$ in magmas and xenoliths as evidence for a single mantle source that dominates the $^3He/^4He$ signal. The $^3He/^4He$ of the metasomatized xenoliths may ultimately be accounted for by an asthenospheric source.

The most likely source for He within these xenoliths is metasomatic fluids related to ongoing continental magmatism. Continental alkali basalt volcanism appears to be preceded in many cases by the infiltration of volatile-rich fluids (H_2O or CO_2-rich) into the lithosphere (e.g., Menzies, 1990). This infiltration leads to modification of the SCLM prior to the arrival of any melt (e.g. Menzies and Murthy, 1980; Wallace and Green, 1988), as well as to the potential for increased partial melting. Development of a flow front of mantle metasomatic fluid (MMF) is a natural consequence of "magma heat death" within the lithosphere (Spera, 1981). Prior to any magma generation within the SCLM, the $^3He/^4He$ of the MMF will strongly overprint the local lithosphere through volatile diffusion, and reset it to an upper mantle $^3He/^4He$ signature. Diffusive equilibration between pre-existing fluid inclusions

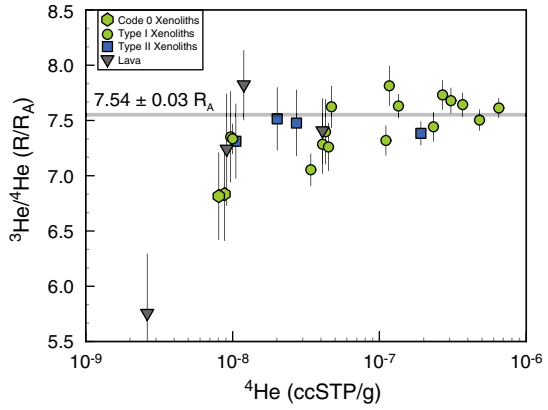

Fig. 4. $^3He/^4He$ (R/R_A) against [^{4}He] (ccSTP/g) for Harrat Hutaymah mineral separates. Green hexagons represent diopside of code 0 xenoliths, green circles represent type I xenolith diopside, enstatite, and amphibole. Blue squares are type II xenolith augite separates and grey triangles are olivine phenocrysts from lava samples. The weighted mean value for all xenoliths, excluding the code 0 samples, is displayed with a grey bar. All helium data was obtained through *in vacuo* crushing. Error bars represent 2σ uncertainty.

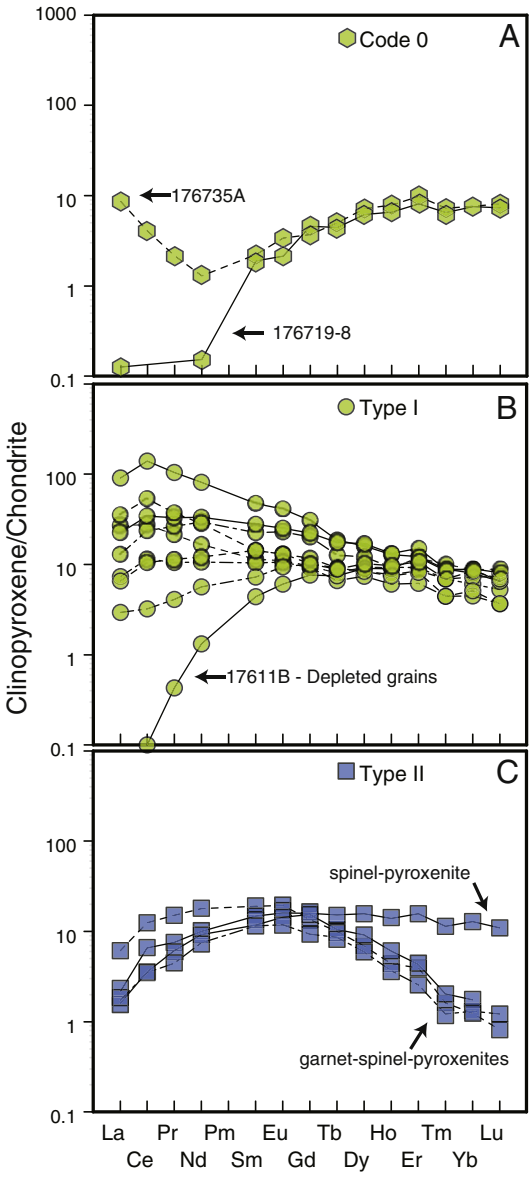

Fig. 3. Chondrite-normalized rare earth element patterns for clinopyroxene grains. Normalizing values are from McDonough and Sun (1995). A) Code 0 diopside. B) Clinopyroxene from type I xenoliths. The averaged LREE depleted grains (n = 2) from sample 17611B is noted while the enriched grain from that sample falls within the array of the type I clinopyroxene (see text for details). C) Augite from type II xenoliths. See text for discussion of xenolith types and codes.

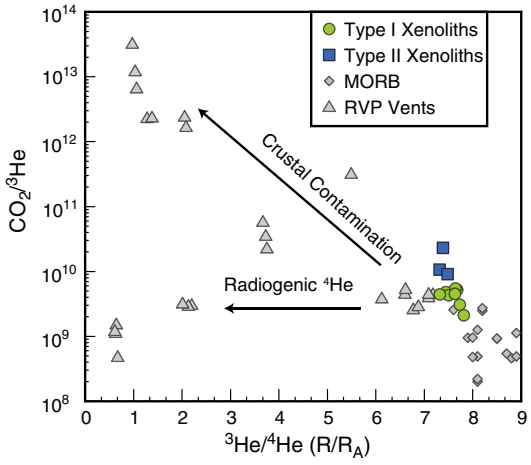

Fig. 5. $CO_2/^3He$ (molar ratio) versus $^3He/^4He$ (R/R_A) for Harrat Hutaymah xenoliths, along with values from a range of MORB vesicles (diamonds; Marty and Zimmermann, 1999) and fluids and gases from vents on the Rungwe Volcanic Province in Tanzania (triangles; Barry et al., 2013). Arrows illustrate the effects radiogenic ^{4}He addition and crustal contamination.

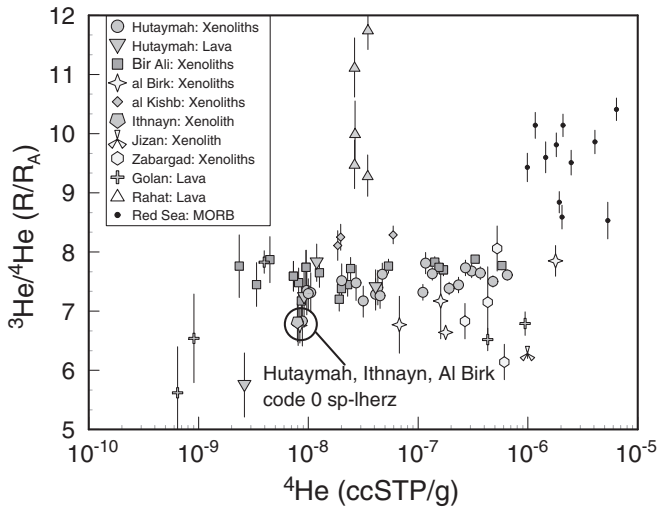

Fig. 6. $^3He/^4He$ (R/R_A) against [^4He] (ccSTP/g) for this study compared to previously published results from the region. Data set includes subaerial lava flows, submarine basalts, and xenoliths. All errors are reported with 2σ uncertainty. Hutaymah results are those shown in Fig. 4, with symbols delimiting xenoliths (circles) vs. lava (inverted triangles). Additional data from Al Kishb, Al Birk, and Ithanyn (Table 3) are also included. Data from Hopp et al. (2004) are total crushed values from pyroxenes and whole rock separates. Data from Torfstein et al. (2013) for the Dead Sea Rift are for olivine and pyroxene separated from Golan basalts. Rahat data are for olivine phenocrysts from Murcia et al. (2013). Bir Ali xenoliths are from Sgualdo et al. (2015). Red Sea data are for submarine basalt glasses reported by Moreira et al. (1996).

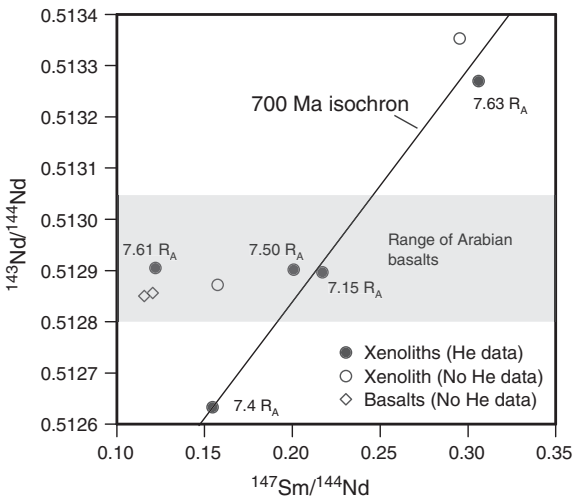

Fig. 7. A Sm-Nd isochron plot after Thornber (1992), with $^3He/^4He$ values denoted next to each symbol where available. The 700 Ma isochron reference line assumes a depleted asthenospheric origin. The range of Arabian basalts is shown as a grey box as a reference for regional young $^{143}Nd/^{144}Nd$ values (data from Stein and Hofmann, 1992; Baker et al., 1997; Bertrand et al., 2003).

and the infiltrating fluids is not strongly favored based on partitioning considerations (Dunai and Porcelli, 2002; Trull and Kurz, 1993), given that He must first undergo transport from a favored host phase (the fluid) into a less favored phase (solid mineral lattice). However, crystalline deformation accompanying fluid infiltration will likely enhance this re-equilibration significantly (e.g. Natland, 2003). There is evidence that this process occurred beneath Hutaymah from the progression of deformation fabrics reported among the type I and II xenoliths (Thornber, 1992, 1994).

The $^3He/^4He$ homogeneity of Hutaymah xenoliths might also result from continuous decrepitation and annealing of inclusions during xenolith transport in the host magma as it ascends and decompresses. Fluid inclusions in mantle xenoliths may contain overpressures of 1 GPa or greater (Andersen and Neumann, 2001; Roedder and Ribbe, 1984), but extensive experimental work on the mineral types in this study shows that the preservation of fluid inclusions from depths greater than ~25 km are uncommon (Roedder and Ribbe, 1984). Fluid inclusion decrepitation will act to drive volatile re-equilibration with the host lava before their re-annealing and subsequent volatile trapping. Hutaymah xenoliths show linear bands of fluid inclusions within pyroxenes and amphiboles (Fig. 2), consistent with a secondary origin for the inclusions (Andersen and Neumann, 2001; Roedder and Ribbe, 1984). The incorporation of host magmatic volatiles into grain boundaries and defects in xenolithic minerals may also have contributed to the observed $^3He/^4He$ homogeneity. This effect has overwhelmed the original (older, lower) $^3He/^4He$ signature of the respective xenolith types with the possible exception of the protogranular spinel lherzolites. Fig. 7 illustrates this process at Hutaymah. A narrow range of $^3He/^4He$ between 7.2 and 7.6 R_A is measured in xenoliths having both Proterozoic ages (those lying on or near the 700 Ma Sm-Nd isochron) and young ages (those displaced to lower Sm/Nd at $^{143}Nd/^{144}Nd$ of 0.5129). Much of the observed 'decoupling' between He isotopes and lithophile isotope signatures in xenoliths sampled globally (e.g. Dunai and Baur, 1995; Dunai and Porcelli, 2002; Stone et al., 1990; Vance et al., 1989) might also be attributed to this type of re-equilibration process.

5.2. Distinguishing Proterozoic and Cenozoic signatures beneath Harrat Hutaymah

Clinopyroxenes in Hutaymah xenoliths analyzed here (including several diopside grains in type I samples, and a single augite from a type II sample) mostly display flat to light rare earth element (LREE) enriched patterns (Fig. 3). A single type I xenolith (176611B) contains both depleted and enriched patterns. Three diopside grains were analyzed from that sample with two containing LREE depletion and one grain showing LREE enrichment similar to that observed in the other type I xenoliths. It is uncertain at this time whether this LREE enrichment signature is representative of an incomplete metasomatic reaction in the entrained xenolith. None of the type I xenoliths analyzed in Thornber (1992) contained a depleted pattern like that observed in this sample; however the bulk rock INAA analyses may not reflect heterogeneity between low trace element concentration 'depleted' grains and high concentration 'enriched' grains. Significantly, no other grains analyzed in this study contained the same pattern as the two depleted diopside grains. Type II augite grains from garnet-bearing pyroxenites show depletion in heavy REEs, consistent with the presence of garnet in the bulk xenolith. The LREE-enriched pyroxenes are consistent with overprinting by a metasomatic agent, as described by Thornber (1992) based on textures, mineralogy and bulk rock chemistry. Similar metasomatic effects have been observed elsewhere on the Arabian Plate (e.g. Blusztajn et al., 1995; Coleman et al., 1983; Krienitz and Haase, 2011; Shaw et al., 2007).

In addition to the tight clustering of $^3He/^4He$ from 7.3 to 7.8 R_A, diopside in the type I xenoliths have a relatively narrow range of $CO_2/^3He$ from 4×10^9 to 5×10^9 (Fig. 5). This range lies at the upper end of the range observed in mid-ocean ridge basalts (Graham et al., 2014a, b; Lupton et al., 2015; Marty and Zimmermann, 1999). Given that their $^3He/^4He$ are within the range of MORBs erupted away from ocean island hotspots, the metasomatic agent responsible for the $^3He/^4He$ homogeneity most likely ultimately originates from the asthenosphere. There is no evidence for any significant contamination of the $^3He/^4He$ or $CO_2/^3He$ by crustal sources like that observed in gases and fluids at the Rungwe Volcanic Province (RVP) vents in the East African Rift (Barry et al., 2013; Fig. 5). Augite grains from the type II garnet-spinel-pyroxenites contain distinctly higher $CO_2/^3He$, ranging above 10^{10} (Table 1). These higher $CO_2/^3He$ values are trending toward those observed in volcanic arc environments, which range above 10^{11} (Fischer

and Marty, 2005; Lupton et al., 2015). These samples experienced Proterozoic deep-crustal metamorphism based on petrology and REE patterns, and they have lithophile isotopic signatures (Thornber, 1992) similar to Proterozoic metamorphic xenoliths from Harrat Lunayyir and Al Kishb (Henjes-Kunst et al., 1990; McGuire and Stern, 1993). It is tempting to associate the elevated $CO_2/^3He$ in type II xenoliths with sub-arc cumulates that may have comprised parts of the ancient Arabian lithospheric mantle, because such garnet pyroxenites have been suggested to represent cumulates of hydrous mafic magmas (e.g., Lee et al., 2006). However, it is unclear how they would have maintained their elevated $CO_2/^3He$ during any subsequent metasomatic alteration, given the much higher He and CO_2 concentrations that are observed in many of the type I xenoliths. It seems more plausible that the higher $CO_2/^3He$ and lower He contents in these deep crustal Proterozoic websterites results from He/CO_2 fractionation, possibly due to preferential loss of He, prior to or following the most recent metasomatic overprinting. The type II xenoliths are inferred to originate near the MOHO based on mineralogy, experimental constraints and thermobarometric calculations (Thornber, 1994). It is therefore possible that these samples experienced some hydrothermal interaction that may fractionate He from CO_2 and generate elevated $CO_2/^3He$ values (e.g. Barry et al., 2013). This hypothesis requires hydrothermal activity to extend to depths of the MOHO (35–40 km; Al-Damegh et al., 2005), which we consider unlikely. Variable $CO_2/^3He$ in the metasomatic fluid might also be produced by a change in the solubility of CO_2 compared to He due to variations in pressure and temperature, but we have no additional information at the present time that suggests this occurred.

Diopside separates from the anhydrous lherzolite (code 0) xenoliths stand in marked contrast to clinopyroxene from the other sample groups, and they show no obvious petrologic evidence of metasomatism (Thornber, 1992). One of them (sample 176719-8) has a clear depleted LREE pattern, consistent with an origin as a melting residue. A second example (176735A) has similar mid-heavy REE abundances (Sm-Yb), but the LREEs from Nd to La become increasing enriched, leading to an overall trough-shaped pattern (Fig. 3). These different REE patterns in the anhydrous lherzolites compared to the other xenoliths are accompanied by the lowest $^3He/^4He$ at Hutaymah (6.8 R_A) and low He concentrations. This suggests that the metasomatic agent responsible for the similarly high values of $^3He/^4He$ (~7.55 ± 0.03 R_A) in both type I and type II had a much reduced, if any, effect on the He isotope character of the anhydrous lherzolites. One way in which these anhydrous lherzolites may have avoided a strong overprinting could be that they were shielded from the penetrating effects of mantle metasomatic fluid because they are derived from the cores of larger modified xenoliths during entrainment. In the case of anhydrous lherzolite sample 176735A, the xenolith was an unusually large specimen at 12,000 cm^3 in estimated volume (~23 cm radius). This sample has $^3He/^4He$ of 6.8 R_A, although it is the example showing a U-shaped REE pattern.

A $^3He/^4He$ value of ~6.8 R_A is commonly observed in xenoliths from other Arabian localities such as Al Birk and Ithnayn, along with exhumed lithospheric mantle on Zabargad Island (Fig. 6). Given their large spatial distribution it seems that these samples might represent the ambient Proterozoic lithospheric mantle beneath the Arabian Plate (Fig. 8). This value of 6.8 R_A appears to be slightly elevated compared to a proposed SCLM end-member value of 6.3 R_A that was observed in a single sample from Jizan (Hopp et al., 2004). Similar or slightly lower values (down to 5.6 R_A) were also measured in olivine phenocrysts from lava flows to the far north in the Golan (Torfstein et al., 2013), but the most helium-rich samples from that region have [He] > 100 nccSTP/g and also show a narrow range of 6.5–6.8 R_A. In places where the SCLM beneath the Arabian Plate has remained largely unmodified by metasomatic effects, it seems to be only slightly heterogeneous in $^3He/^4He$, showing a narrower range than the typically accepted values for SCLM globally (~6 ± 2 R_A: Day et al., 2005; Dunai and Porcelli, 2002).

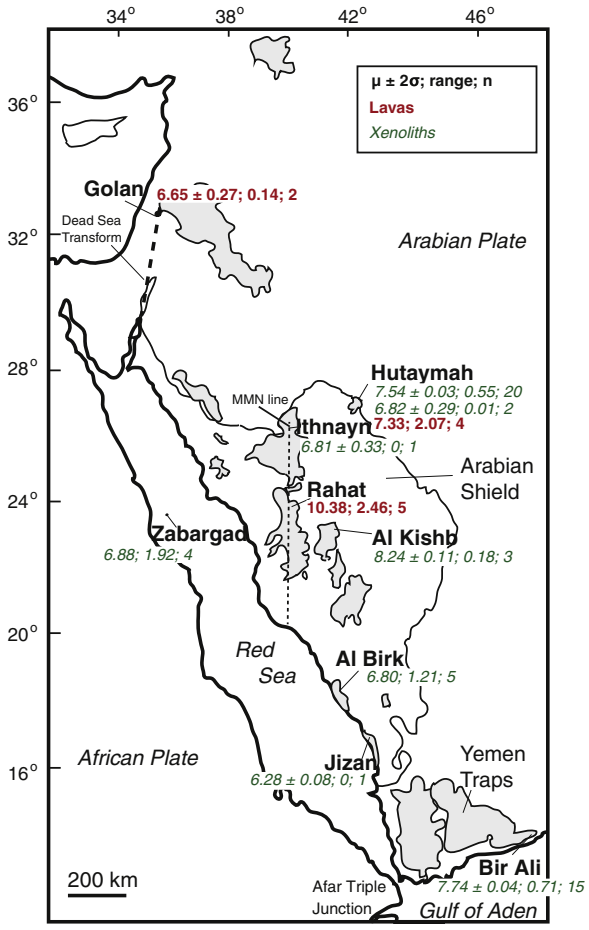

Fig. 8. Regional map of the Arabian Plate with volcanic fields shown in grey. Numbers relate to the measured $^3He/^4He$. The values reported are the weighted mean $^3He/^4He$ ± its uncertainty: the range of $^3He/^4He$ (highest–lowest measured value): and the number of samples. For locations with a large range (>1 R_A), a weighted mean value is not an accurate characterization. The weighted mean (μ) is $\mu = \sum(x_i/\sigma_i^2)/\sum(1/\sigma_i^2)$, where x_i is the $^3He/^4He$ of sample i and σ_i represents its associated analytical uncertainty. The weighted mean error is $\sigma_\mu = [1/\sum(1/\sigma_i^2)]^{0.5}$ (Bevington, 1969). The reported ranges are the differences between the maximum and minimum $^3He/^4He$ (R/R_A) for a given harrat. Harrat Hutaymah is shown with two xenolith averages; the top (n = 20) represents all non-code 0 xenoliths while the second set of values represents just code 0 xenoliths (see text for discussion). Other data sources are: Golan (only samples with [^4He] > 100 nccSTP/g are used), Torfstein et al. (2013); Rahat, Murcia et al. (2013); Zabargad, Jizan and Al Birk, Hopp et al. (2004) (excluding values measured by step heating); Bir Ali, Sgualdo et al. (2015). Hutaymah, Ithnayn, Al Kishb, and one Al Birk sample are from this study. The MMN line represents the Makkah-Medinah-Nafud lineament characterized by increased volcanism and thinner lithosphere.

5.3. Metasomatic and volcanic sources in Western Arabia

There is a covariation between LREE enrichment, exemplified by La/Yb, and He concentration in xenoliths from Arabia as well as a suite studied by Sgualdo et al. (2015) from Yemen (Fig. 9A). This covariation suggests that the source of He in the xenoliths having $^3He/^4He$ of ~7.3–7.8 R_A is a trace element-enriched mantle source. The $^3He/^4He$ values further suggest that this source for helium is ultimately the underlying asthenosphere as discussed above. However, the degree of trace element enrichment observed in the xenoliths (Fig. 3) is not readily accounted for by melts from a depleted asthenospheric source, even at very low degrees of partial melting that would give rise to alkaline magmas or metasomatic fluids. We therefore suggest that the source of the mantle metasomatic fluid originates through hybridization of material from the continental lithospheric mantle (± crust) and the asthenosphere. This could occur either through lithospheric delamination

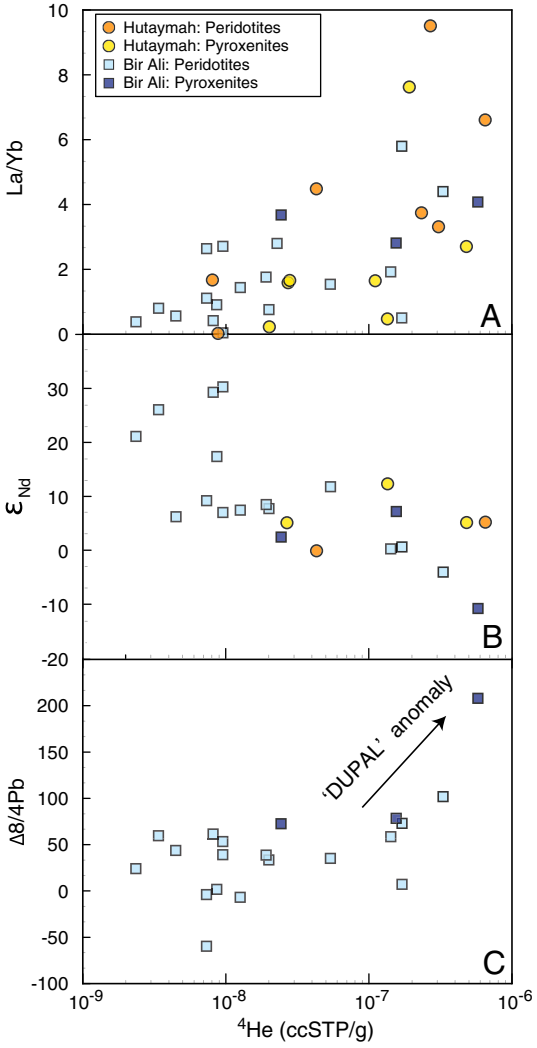

Fig. 9. A) La/Yb versus [He] (ccSTP/g) from Hutaymah clinopyroxenes and Bir Ali xenoliths (Sgualdo et al. 2015). La/Yb in Bir Ali samples was measured through mineral dissolution ICP-MS, while the Hutaymah samples were analyzed using LA-ICP-MS. B) ε_{Nd} versus [He] (ccSTP/g), with Hutaymah Nd isotopic values from Thornber (1992). C) Δ8/4Pb versus [He] (ccSTP/g) from Bir Ali xenoliths (data from Sgualdo et al., 2015). Δ8/4Pb is from Hart (1984) and is defined as $100*[^{208}Pb/^{204}Pb - 1.209\ (^{206}Pb/^{204}Pb) + 15.627)]$. This parameter is a measure of ancient Th/U fractionation and the tendency of isotopic domains to be more similar to those sampled from beneath the Indian Ocean compared to other regions like the Atlantic or Pacific.

and mixing/melting with the ambient upper mantle during rifting (Arndt and Goldstein, 1989; Elkins-Tanton, 2007), or from open-system behavior of an enriched mantle layer immediately underlying the SCLM, a so-called "perisphere" (Anderson, 1995).

The covariation of He concentration with La/Yb in xenoliths from both Saudi Arabia and from Yemen (Sgualdo et al., 2015) are quite similar (Fig. 9A). The Yemen xenoliths are from diatremes in Bir Ali and contain similar He isotopic signatures (7.2–7.9 R_A; Sgualdo et al., 2015) to those found at Hutaymah. In addition, the Nd isotopic compositions of Yemen samples reveal a strong relationship between ε_{Nd} (range +30.3 to −10.5) and He concentration (correlations also exists for Pb and Hf isotopes). The helium concentration may therefore be viewed as a proxy for the amount of metasomatic fluid trapped in the xenoliths, and indicates that the metasomatic agent beneath Yemen has $\varepsilon_{Nd} < -10$ (Sgualdo et al., 2015). The ε_{Nd} range for Hutaymah xenoliths is considerably narrower, between −0.1 and +14 (n = 10; Thornber, 1992), and there is no clear trend with [He] in the four samples analyzed here. The range of Nd isotope compositions implicates ancient continental crust and lithosphere. Model ages corresponding to ε_{Nd} of -10 assuming a typical crustal Sm/Nd (~40% lower than BSE) are T_{CHUR} = 800 Ma and T_{DM} = 1400 Ma (DePaolo, 1981). This ancient material could have been reworked down to basal levels of the lithosphere or the shallowest asthenosphere during Pan-African orogeny and the final amalgamation of Gondwana, followed by more recent reactivation and its involvement as a geochemical component in the harrat volcanism during recent (<30 Ma) rifting.

Further evidence for the nature of this enriched end-member comes from consideration of Δ8/4Pb in the Yemen xenoliths and their He contents (Fig. 9B). Δ8/4Pb is a parameter defined by Hart (1984) and represents the vertical deviation from a Northern Hemisphere Reference Line in a $^{208}Pb/^{204}Pb$-$^{206}Pb/^{204}Pb$ diagram. Δ8/4Pb is a measure of so-called Dupal mantle, a mega-scale isotope anomaly displayed by South Atlantic and Indian Ocean basalts. The metasomatic agent at Yemen is most strongly observed in the websterites, which have an end-member Δ8/4Pb ranging from +75 to > +200 (Fig. 9B), which is more extreme than Δ8/4Pb values observed in any ocean basins (e.g. Janney et al., 2005; Kamenetsky et al., 2001). This provides compelling evidence for association of the Dupal anomaly with upper mantle contamination by ancient sub-continental lithospheric mantle.

This type of upper mantle contamination has been discerned previously from the Pb isotope variations in Quaternary volcanic rocks from the Main Ethiopian Rift (MER), where there is a strong interaction between the Afar mantle plume and the local Pan-African lithosphere (Rooney et al., 2012). The Pb isotope evidence from the MER reveals that the mantle plume interacts with the local continental lithosphere and shallow asthenosphere (mid-ocean ridge basalt-like source) through an ordered sequence of events. First the continental lithosphere becomes detached and mixed into the shallow mantle, and then upwelling plume material (plus entrained lithosphere) can flow beneath the developing rift system, metasomatizing and potentially melting the SCLM. Metasomatism of the SCLM increases its gravitational instability and tendency to begin to erode (e.g. Elkins-Tanton, 2007; Wang et al., 2015). Following this reasoning, we suggest that the enriched source beneath the Arabian Plate was produced by hybridization between subjacent asthenospheric mantle and reworked continental lithosphere during the early stages of lithospheric thinning along the Makkah-Medinah-Nafud (MMN) line prior to ~12 Ma. Fig. 10 illustrates this schematically, showing a thinning of the lithosphere beneath the MMN line, likely from an upwelling plume or entrained enriched plume material (evident from the elevated $^3He/^4He$ found at Rahat; Murcia et al., 2013). As the lithospheric erosion progresses, asthenospheric mantle will rise to replace the lithosphere. Eventually this delaminated SCLM may devolatize and/or partially melt (Elkins-Tanton, 2007; Wang et al., 2015), creating a hybridized (asthenospheric $^3He/^4He$ and low εNd and εHf) metasomatic fluid.

The role of Afar plume material in the regional metasomatism remains enigmatic. The delamination of SCLM may have been driven by flow of Afar plume material at depth, but the currently available isotopic evidence suggests that the plume has not significantly contributed to the generation of harrat magmas based on comparisons of the isotopic compositions of harrat basalts (e.g. Altherr et al., 1990; Bertrand et al., 2003; Stein and Hofmann, 1992) with Ethiopian flood basalts (Kieffer et al., 2004; Pik et al., 1999) and Yemen flood basalts (Baker et al., 1997). Lithospheric thinning and delamination accompanied by small-scale convective instabilities (e.g., Burov and Gerya, 2014) would have stirred the depleted asthenospheric and enriched basal lithospheric components together. The presence of the Afar plume in the south and subduction at the Hellenic trench in the north leads to large scale anti-clockwise rotation of the Arabian Plate, and lateral flow to the east at mantle depths of 100–400 km beneath the region of harrat volcanism (Faccenna et al., 2013, see their Fig. 4F). This lateral flow of asthenospheric mantle from beneath the thinned shield underlying the MMN lineament toward thicker lithosphere to the east would transport this hybridized source material to beneath Hutaymah (Fig. 10) where it has been involved in the young metasomatism and volcanism of that

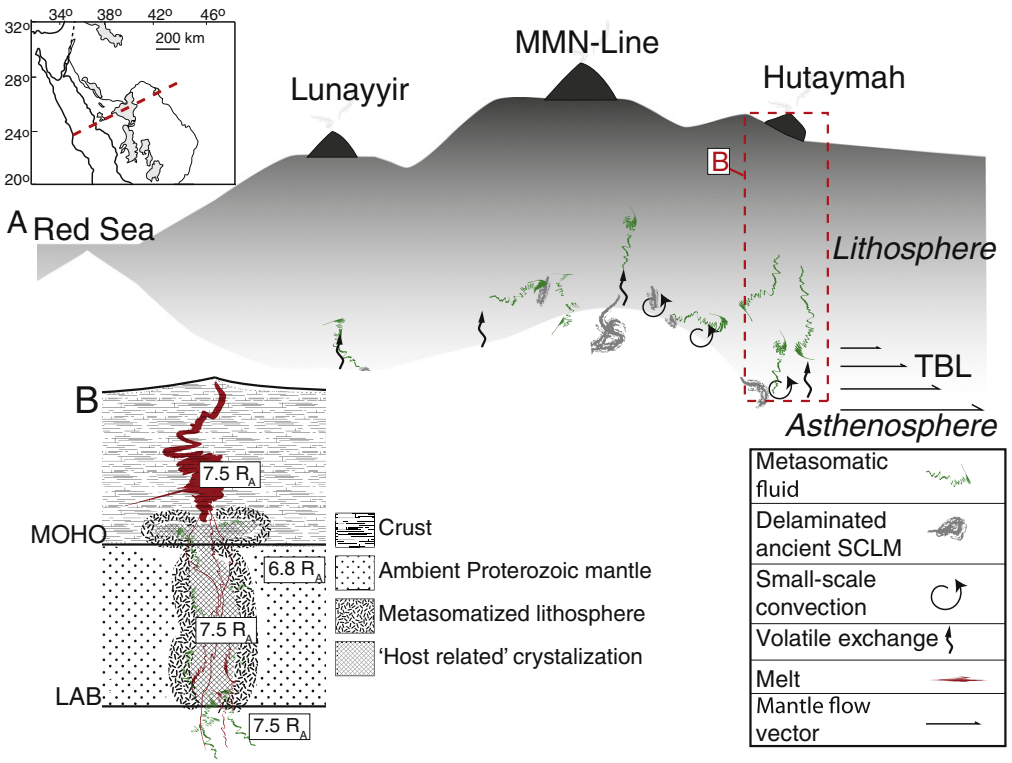

Fig. 10. A) Cartoon cross section going from the Red Sea to Harrat Hutaymah. The scale is schematic to show features. The thermal boundary layer (TBL) contains convective stirring of enriched, delaminated lithosphere with asthenosphere beneath the MMN line and eastward transport in an enriched sub-lithosphere layer to the lithosphere-asthenosphere boundary beneath Hutaymah. B) A schematic representation of lithosphere beneath Hutaymah. Unaltered country rocks represent 'code 0' type lithologies although this may not be limited to spinel lherzolites. The diagram is based upon the lithosphere zones of Thornber (1994).

area (<850 ka). The ancient lithospheric component is clearly observed in the Pb and Nd isotope compositions of hybridized enriched sources such as the Bir Ali xenoliths in Yemen, while the He isotopes appear to be more strongly leveraged by the asthenospheric input resembling the effects seen at both Hutaymah and Bir Ali. It is important to note that the low ε_{Nd} (-10.5) for the metasomatic agent beneath Yemen is also well outside of the range of values observed in Afar plume material (ε_{Nd} +4 to +6; Meshesha and Shinjo, 2008; Pik et al., 2006; Rooney et al., 2012). The He concentrations (this study) and $^{143}Nd/^{144}Nd$ values for four Hutaymah xenoliths (Thornber, 1992) also appear to roughly fit the trend for Bir Ali xenoliths outlined in Sgualdo et al. (2015) although the Hutaymah range is much less. Further tests of the plume-lithosphere-asthenosphere hybridization model could be obtained through Pb and Hf isotope analyses of Hutaymah xenoliths.

Other models have been proposed for the origin of Arabian volcanism. These include reactivation of fossil plume head material during lithospheric extension (Stein and Hofmann, 1992), and melting of Afar plume material as it is channeled northward beneath western Arabia (Camp and Roobol, 1992; Chang and Van der Lee, 2011). Stein and Hofmann (1992) suggested that the enriched isotopic composition of harrat basalts and their lack of a clear age progression were caused by reactivation of ancient fossil plume material within the Arabian lithosphere. However, others have argued that the radiogenic Pb isotope compositions in Arabian basalts result from melting of heterogeneous lithospheric mantle (Blusztajn et al., 1995; Rooney et al., 2014; Shaw et al., 2003; Shaw et al., 2007). Most basalts and xenoliths north of Yemen appear to be better explained by involvement of continental lithosphere rather than a young or fossil plume. One exception is at Rahat, where $^3He/^4He$ in young lava flows extend to 11.8 R_A (Murcia et al., 2013), and possibly to higher values in other (older?) volcanic formations associated with the MMN line where thinner lithosphere and higher mantle potential temperatures are observed (Camp and Roobol, 1992). In this context it is notable that a single xenolith from Ithnayn to the north of Rahat has a $^3He/^4He$ of 6.8 R_A (Table 3; Fig. 6) indicating a lithospheric source. Seismic tomography reveals a velocity anomaly stretching from the Afar triple junction northward towards Turkey that appears to link this mantle feature at 100–300 km beneath western Arabia to the Afar mantle plume (Chang and Van der Lee, 2011; Hansen et al., 2006). However, harrat volcanism appears to be driven by melts originating near the lithosphere-asthenosphere boundary (e.g. Bertrand et al., 2003; Duncan and Al-Amri, 2013; Shaw et al., 2003; Thornber, 1992), and the Afar mantle plume does not appear to represent a significant source in most cases.

6. Conclusions

$^3He/^4He$ in xenoliths from Harrat Hutaymah are remarkably homogeneous at 7.3–7.8 R_A, with exception of the anhydrous lherzolites that are distinctly lower at 6.8 R_A. The homogeneity of $^3He/^4He$ at 7.54 R_A appears to result from infiltration of vapor-saturated magmas along crystalline grain boundaries within the xenoliths. Collectively, the $^3He/^4He$, xenolith and lava flow compositions (Thornber, 1992), and trace element systematics for the xenolith mineral phases indicate an origin from volatile-rich metasomatic melt formed by small degree (~5%) partial melting of mantle near the lithosphere-asthenosphere boundary. The lower $^3He/^4He$ values of ~6.8 R_A are similar to those commonly observed in other harrats, and appear to represent pre-existing ambient lithospheric mantle unaffected by metasomatism. The origin of magmas and metasomatic fluids in the young volcanism of western Arabia and Yemen can be accounted for by a hybrid mantle source that formed by admixing of ancient enriched lithospheric mantle and shallow depleted mantle asthenosphere. The role of the Afar plume in volcanism throughout the region remains somewhat enigmatic; while its presence beneath the region is inferred from seismic imaging and

topographic uplift, its involvement as a magma source appears to be minor based on the available geochemical evidence.

Acknowledgments

We thank Dr. Saeed Alshaltoni for assistance in the field. Richard Bradshaw provided valuable assistance with the LA-ICP-MS analysis. Jurek Blusztajn kindly provided the xenolith material from Al Kishb, Ithnayn and Al Birk. We thank Peter Barry, Mark Stelten, and an anonymous reviewer for constructive reviews that improved the manuscript. This study was supported by funds from the National Science Foundation through grants OCE 12-59964 and EAR 15-24675.

Appendix A. Supplementary data

Supplementary data to this article can be found online at http://dx.doi.org/10.1016/j.lithos.2016.01.031.

References

Albarède, F., 2003. The thermal history of leaky chronometers above their closure temperature. Geophysical Research Letters 30, 15-1–15-4.
Al-Damegh, K., Sandvol, E., Barazangi, M., 2005. Crustal structure of the Arabian plate: new constraints from the analysis of teleseismic receiver functions. Earth and Planetary Science Letters 231 (3), 177–196.
Altherr, R., Henjes-Kunst, F., Baumann, A., 1990. Asthenosphere versus lithosphere as possible sources for basaltic magmas erupted during formation of the Red Sea: Constraints from Sr, Pb and Nd isotopes. Earth and Planetary Science Letters 96, 269–286.
Andersen, T., Neumann, E.-R., 2001. Fluid inclusions in mantle xenoliths. Lithos 55, 301–320.
Anderson, D.L., 1995. Lithosphere, asthenosphere, and perisphere. Reviews of Geophysics 33, 125–149.
Arndt, N.T., Goldstein, S.L., 1989. An open boundary between the lower continental crust and mantle: its role in crust formation and crust recycling. Tectonophysics 161, 2011–2212.
Bailey, D., 1982. Mantle metasomatism-continuing chemical change within the Earth. Nature 296, 525–530.
Baker, J.A., Menzies, M.A., Thirlwall, M.F., Macpherson, C.G., 1997. Petrogenesis of Quaternary intraplate volcanism, Sana'a, Yemen: implications for plume-lithosphere interaction and polybaric melt hybridization. Journal of Petrology 38, 1359–1390.
Barry, P.H., Hilton, D.R., Fischer, T.P., de Moor, J.M., Mangasini, F., Ramirez, C., 2013. Helium and carbon isotope systematics of cold "mazuku" CO 2 vents and hydrothermal gases and fluids from Rungwe Volcanic Province, southern Tanzania. Chemical Geology 339, 141–156.
Barry, P.H., Hilton, D.R., Day, J.M.D., Pernet-Fisher, J.F., Howarth, G.H., Magna, T., Agashev, A.M., Pokhilenko, N.P., Pokhilenko, L.N., Taylor, L.A., 2015. Helium isotopic evidence for modification of the cratonic lithosphere during the Permo-Triassic Siberian flood basalt event. Lithos 216–217, 73–80.
Bedini, R.M., Blichert-Toft, J., Boyet, M., Albarède, F., 2004. Isotopic constraints on the cooling of the continental lithosphere. Earth and Planetary Science Letters 223, 99–111.
Bertrand, H., Chazot, G., Blichert-Toft, J., Thoral, S., 2003. Implications of widespread high-μ volcanism on the Arabian Plate for Afar mantle plume and lithosphere composition. Chemical Geology 198, 47–61.
Bevington, P.R., 1969. Data Reduction and Error Analysis for the Physical Sciences. McGraw-Hill, New York (336 pp.).
Blusztajn, J., Hart, S., Shimizu, N., McGuire, A., 1995. Trace-element and isotopic characteristics of spinel peridotite xenoliths from Saudi Arabia. Chemical Geology 123, 53–65.
Bohannon, R.G., Naeser, C.W., Schmidt, D.L., Zimmermann, R.A., 1989. The timing of uplift, volcanism, and rifting peripheral to the Red Sea: a case for passive rifting? Journal of Geophysical Research - Solid Earth 94, 1683–1701 (1978–2012).
Burnard, P.G., Stuart, F., Turner, G., 1994. C, He, Ar variations within a dunite nodule as a function of fluid inclusion morphology. Earth and Planetary Science Letters 128 (3), 243–258.
Burnard, P.G., Demouchy, S., Delon, R., Arnaud, N.O., Marrocchi, Y., Cordier, P., Addad, A., 2015. The role of grain boundaries in the storage and transport of noble gases in the mantle. Earth and Planetary Science Letters 430, 260–270.
Burov, E., Gerya, T., 2014. Asymmetric three-dimensional topography over mantle plumes. Nature 513, 85–92.
Camp, V.E., Roobol, M.J., 1992. Upwelling asthenosphere beneath western Arabia and its regional implications. Journal of Geophysical Research - Solid Earth 97, 15255–15271 (1978–2012).
Chang, S.-J., Van der Lee, S., 2011. Mantle plumes and associated flow beneath Arabia and East Africa. Earth and Planetary Science Letters 302, 448–454.
Coleman, R.G., Gregory, R., Brown, G.F., Arabia, S., 1983. Cenozoic volcanic rocks of Saudi Arabia. US Department of the Interior, Geological Survey.
Darrah, T.H., Tedesco, D., Tassi, F., Vaselli, O., Cuoco, E., Poreda, R.J., 2012. Gas chemistry of the Dallol region of the Danakil Depression in the Afar region of the northern-most East African Rift. Chemical Geology 339, 16–29.
Day, J.M., Hilton, D.R., Pearson, D.G., Macpherson, C.G., Kjarsgaard, B.A., Janney, P.E., 2005. Absence of a high time-integrated $^{3}He/(U+Th)$ source in the mantle beneath continents. Geology 33, 733–736.
Day, J.M., Barry, P.H., Hilton, D.R., Burgess, R., Pearson, D.G., Taylor, L.A., 2015. The helium flux from the continents and ubiquity of low $^{3}He/^{4}He$ recycled crust and lithosphere. Geochimica et Cosmochimica Acta 153, 116–133.
DePaolo, D.J., 1981. Neodymium isotopes in the Colorado Front Range and crust-mantle evolution in the Proterozoic. Nature 291, 193–196.
Dunai, T., Baur, H., 1995. Helium, neon, and argon systematics of the European subcontinental mantle: Implications for its geochemical evolution. Geochimica et Cosmochimica Acta 59, 2767–2783.
Dunai, T.J., Porcelli, D., 2002. Storage and transport of noble gases in the subcontinental lithosphere. Reviews in Mineralogy and Geochemistry 47, 371–409.
Duncan, R.A., Al-Amri, A.M., 2013. Timing and composition of volcanic activity at Harrat Lunayyir, western Saudi Arabia. Journal of Volcanology and Geothermal Research 260, 103–116.
Duncan, R.A., Kent, A.J.R., Thornber, C.R., Schlieder, T.D., Al-Amri, A.M., 2016. Timing and composition of continental volcanism at Harrat Hutaymah, western Saudi Arabia. Journal of Volcanology and Geothermal Research http://dx.doi.org/10.1016/j.jvolgeores.2016.01.010.
Elkins-Tanton, L., 2007. Continental magmatism, volatile recycling and a heterogeneous mantle caused by lithospheric gravitational instabilities. Journal of Geophysical Research - Solid Earth 112 (B3) (1978–2012).
Faccenna, C., Becker, T.W., Jolivet, L., Keskin, M., 2013. Mantle convection in the Middle East: Reconciling Afar upwelling, Arabia indentation and Aegean trench rollback. Earth and Planetary Science Letters 375, 254–269.
Fischer, T.P., Marty, B., 2005. Volatile abundances in the sub-arc mantle: insights from volcanic and hydrothermal gas discharges. Journal of Volcanology and Geothermal Research 140, 205–216.
Graham, D.W., 2002. Noble gas isotope geochemistry of mid-ocean ridge and ocean island basalts: characterization of mantle source reservoirs. Reviews in Mineralogy and Geochemistry 47, 247–317.
Graham, D.W., Hanan, B.B., Hémond, C., Blichert-Toft, J., Albarède, F., 2014a. Helium isotopic textures in Earth's upper mantle. Geochemistry, Geophysics, Geosystems 15 (5), 2048–2074.
Graham, D.W., Hanan, B.B., Lupton, J.E., Hoernle, K., Werner, R., Christie, D.M., Sinton, J.M., 2014b. Helium isotope variations and mantle plume-spreading ridge interactions along the Galápagos Spreading Center. In: Harpp, K.S., Mittelstaedt, E., d'Ozouville, N., Graham, D.W. (Eds.), The Galápagos: A Natural Laboratory for the Earth Sciences. Geophysical Monograph 204, pp. 393–414.
Halldorsson, S.A., Hilton, D.R., Scarsi, P., Abebe, T., Hopp, J., 2014. A common mantle plume source beneath the entire East African Rift System revealed by coupled helium–neon systematics. Geophysical Research Letters 41, 2304–2311.
Hansen, S., Schwartz, S., Al-Amri, A., Rodgers, A., 2006. Combined plate motion and density-driven flow in the asthenosphere beneath Saudi Arabia: evidence from shear-wave splitting and seismic anisotropy. Geology 34, 869–872.
Hart, S.R., 1984. A large-scale isotope anomaly in the southern hemisphere mantle. Nature 309, 753–757.
Hart, S.R., Kurz, M.D., Wang, Z., 2008. Scale length of mantle heterogeneities: constraints from helium diffusion. Earth and Planetary Science Letters 269, 508–517.
Hempton, M.R., 1987. Constraints on Arabian plate motion and extensional history of the Red Sea. Tectonics 6, 687–705.
Henjes-Kunst, F., Altherr, R., Baumann, A., 1990. Evolution and composition of the lithospheric mantle underneath the western Arabian peninsula: constraints from Sr — Nd isotope systematics of mantle xenoliths. Contributions to Mineralogy and Petrology 105, 460–472.
Hilton, D., Porcelli, D., 2003. Noble gases as mantle tracers. Treatise on Geochemistry 2, 277–318.
Hilton, D.R., Halldórsson, S.A., Barry, P.H., Fischer, T.P., de Moor, J.M., Ramirez, C.J., Mangasini, F., Scarsi, P., 2011. Helium isotopes at Rungwe Volcanic Province, Tanzania, and the origin of East African Plateaux. Geophysical Research Letters 38 (21). http://dx.doi.org/10.1029/2011GL049589.
Hopp, J., Trieloff, M., Altherr, R., 2004. Neon isotopes in mantle rocks from the Red Sea region reveal large-scale plume–lithosphere interaction. Earth and Planetary Science Letters 219, 61–76.
Janney, P.E., Le Roex, A.P., Carlson, R., 2005. Hafnium isotope and trace element constraints on the nature of mantle heterogeneity beneath the central Southwest Indian Ridge (13 E to 47 E). Journal of Petrology 46, 2427–2464.
Kamenetsky, V.S., Maas, R., Sushchevskaya, N.M., Norman, M.D., Cartwright, I., Peyve, A.A., 2001. Remnants of Gondwanan continental lithosphere in oceanic upper mantle: Evidence from the South Atlantic Ridge. Geology 29, 243–246.
Kieffer, B., Arndt, N., Lapierre, H., Bastien, F., Bosch, D., Pecher, A., Yirgu, G., Ayalew, D., Weis, D., Jerram, D.A., Keller, F., 2004. Flood and shield basalts from Ethiopia: magmas from the African superswell. Journal of Petrology 45 (4), 793–834.
Krienitz, M.-S., Haase, K.M., 2011. The evolution of the Arabian lower crust and lithospheric mantle—geochemical constraints from southern Syrian mafic and ultramafic xenoliths. Chemical Geology 280, 271–283.
Krienitz, M.S., Haase, K., Mezger, K., van den Bogaard, P., Thiemann, V., Shaikh-Mashail, M., 2009. Tectonic events, continental intraplate volcanism, and mantle plume activity in northern Arabia: constraints from geochemistry and Ar-Ar dating of Syrian lavas. Geochemistry, Geophysics, Geosystems 10.
Lee, C.-T.A., Cheng, X., Horodyskyj, U., 2006. The development and refinement of continental arcs by primary basaltic magmatism, garnet pyroxenite accumulation, basaltic recharge and delamination: insights from the Sierra Nevada, California. Contributions to Mineralogy and Petrology 151, 222–242.

Loewen, M.W., Kent, A.J., 2012. Sources of elemental fractionation and uncertainty during the analysis of semi-volatile metals in silicate glasses using LA-ICP-MS. Journal of Analytical Atomic Spectrometry 27 (9), 1502–1508.
Lupton, J., Evans, L., 2004. The atmospheric helium isotope ratio: Is it changing? Geophysical Research Letters 31.
Lupton, J., Rubin, K.H., Arculus, R., Lilley, M., Butterfied, D., Resing, J., Baker, E., Embley, R., 2015. Helium isotope, C/^{3}He, and Ba-Nb-Ti signatures in the northern Lau Basin: distinguishing arc, back-arc, and hotspot affinities. Geochemistry, Geophysics, Geosystems 16 (4), 1133–1155.
Marty, B., Zimmermann, L., 1999. Volatiles (He, C, N, Ar) in mid-ocean ridge basalts: assesment of shallow-level fractionation and characterization of source composition. Geochimica et Cosmochimica Acta 63, 3619–3633.
Marty, B., Pik, R., Gezahegn, Y., 1996. Helium isotopic variations in Ethiopian plume lavas: nature of magmatic sources and limit on lower mantle contribution. Earth and Planetary Science Letters 144, 223–237.
Matsuda, J., Matsumoto, T., Sumino, H., Nagao, K., Yamamoto, J., Miura, Y., Kaneoka, I., Takahata, N., Sano, Y., 2002. The ^{3}He/^{4}He ratio of the new internal He Standard of Japan (HESJ). Geochemical Journal-Japan 36, 191–195.
McDonough, W.F., Sun, S.S., 1995. The composition of the Earth. Chemical geology 120 (3), 223–253.
McGuire, A.V., Stern, R.J., 1993. Granulite xenoliths from western Saudi Arabia: the lower crust of the late Precambrian Arbian-Nubian Shield. Contributions to Mineralogy and Petrology 114, 395–408.
Menzies, M.A., 1990. Continental mantle. Oxford Science Publications, p. 184.
Menzies, M., Murthy, V.R., 1980. Mantle metasomatism as a precursor to the genesis of alkaline magmas-isotopic evidence. American Journal of Science 280, 622–638.
Meshesha, D., Shinjo, R., 2008. Rethinking geochemical feature of the Afar and Kenya mantle plumes and geodynamic implications. Journal of Geophysical Research - Solid Earth 113 (1978–2012).
Moore, J.G., Batchelder, J.N., Cunningham, C.G., 1977. CO_2-filled vesicles in mid-ocean basalt. Journal of Volcanology and Geothermal Research 2 (4), 309–327.
Moreira, M., Valbracht, P.J., Staudacher, T., Allègre, C.J., 1996. Rare gas systematics in Red Sea ridge basalts. Geophysical research letters 23 (18), 2453–2456.
Moufti, M.R., Moghazi, A.M., Ali, K.A., 2012. Geochemistry and Sr–Nd–Pb isotopic composition of the Harrat Al-Madinah Volcanic Field, Saudi Arabia. Gondwana Research 21 (2), 670–689.
Murcia, H., Lindsay, J.M., Niedermann, S., Cronin, S.J., Smith, I.E., El-Masry, N.N., Moufti, M.R.H., Németh, K., 2013. The potential use of cosmogenic nuclides for dating in Harrat Rahat. VORISA Scientific Meeting extended abstract, pp. 24–28.
Natland, J.H., 2003. Capture of helium and other volatiles during the growth of olivine phenocrysts in picritic basalts from the Juan Fernandez Islands. Journal of Petrology 44 (3), 421–456.
Pallister, J.S., 1984. Reconnaissance geology of the Harrat Hutaymah quadrangle, sheet 26/42 A. Ministry of Petroleum and Mineral Resources, Deputy Ministry for Mineral Resources, Kingdom of Saudi Arabia.
Pik, R., Marty, B., Hilton, D., 2006. How many mantle plumes in Africa? The geochemical point of view. Chemical Geology 226, 100–114.
Pik, R., Deniel, C., Coulon, C., Yirgu, G., Marty, B., 1999. Isotopic and trace element signatures of Ethiopian flood basalts: Evidence for plume–lithosphere interactions. Geochimica et Cosmochimica Acta 63 (15), 2263–2279.
Roedder, E., Ribbe, P., 1984. Fluid inclusions. Vol. 12. Mineralogical Society of America, Washington, DC.
Rooney, T.O., Hanan, B.B., Graham, D.W., Furman, T., Blichert-Toft, J., Schilling, J.-G., 2012. Upper mantle pollution during Afar Plume–Continental rift interaction. Journal of Petrology 53, 365–389.
Rooney, T.O., Nelson, W.R., Dosso, L., Furman, T., Hanan, B., 2014. The role of continental lithosphere metasomes in the production of HIMU-like magmatism on the northeast African and Arabian plates. Geology 42, 419–422.
Scarsi, P., Craig, H., 1996. Helium isotope ratios in Ethiopian Rift basalts. Earth and Planetary Science Letters 144, 505–516.
Sgualdo, P., Aviado, K., Beccaluva, L., Bianchini, G., Blichert-Toft, J., Bryce, J., Graham, D., Natali, C., Siena, F., 2015. Lithospheric mantle evolution in the Afro-Arabian domain: Insights from Bir Ali mantle xenoliths (Yemen). Tectonophysics 650, 3–17.
Shaw, J.E., Baker, J.A., Menzies, M.A., Thirlwall, M.F., Ibrahim, K.M., 2003. Petrogenesis of the largest intraplate volcanic field on the Arabian Plate (Jordan): a mixed lithosphere–asthenosphere source activated by lithospheric extension. Journal of Petrology 44, 1657–1679.
Shaw, J.E., Baker, J.A., Kent, A.J.R., Ibrahim, K.M., Menzies, M.A., 2007. The geochemistry of the Arabian lithospheric mantle—a source for intraplate volcanism? Journal of Petrology 48, 1495–1512.
Spera, F.J., 1981. Carbon dioxide in igneous petrogenesis: II. Fluid dynamics of mantle metasomatism. Contributions to Mineralogy and Petrology 77, 56–65.
Spera, F.J., 1984. Carbon dioxide in petrogenesis III: role of volatiles in the ascent of alkaline magma with special reference to xenolith-bearing mafic lavas. Contributions to Mineralogy and Petrology 88, 217–232.
Stein, M., 2003. Tracing the plume material in the Arabian-Nubian Shield. Precambrian Research 123, 223–234.
Stein, M., Hofmann, A.W., 1992. Fossil plume head beneath the Arabian lithosphere? Earth and Planetary Science Letters 114, 193–209.
Stern, R.J., Johnson, P., 2010. Continental lithosphere of the Arabian Plate: a geologic, petrologic, and geophysical synthesis. Earth-Science Reviews 101, 29–67.
Stoeser, D.B., Frost, C.D., 2006. Nd, Pb, Sr, and O isotope characterization of Saudi Arabian Shield terranes. Chemical Geology 226, 163–188.
Stone, J., Porcelli, D., Vance, D., Galer, S., O'Nions, R., 1990. Volcanic traces. Nature 346, 228.
Stuart, F.M., 2013. Comparing the composition of the earliest basalts erupted by the Iceland and Afar mantle plumes. Geophysical Research Abstracts 15. EGU, pp. 2013–13389.
Thornber, Carl R., 1990, Geologic map of Harrat Hutaymah, Saudi Arabia, with the petrologic classification and distribution of ultramafic inclusions (1:100,000 scale), USGS Miscellaneous Field Studies Map MF-2129
Thornber, Carl R., 1992. The petrology, geochemistry and origin of ultramafic inclusions and mafic alkaline magmas from Harrat Hutaymah, Saudi Arabia. Open-File Report USGS-OF-92-6. Saudi Arabian Ministry of Petroleum and Mineral resources, Deputy Ministry of Mineral Resources, Jiddah, Kingdom of Saudi Arabia (15 data tables covering 99 pages, 36 figures, 7 photographs and 1 oversize map, 244 pp.).
Thornber, C., 1994. Ultramafic inclusions from Harrat Hutaymah: a record of mantle magmatism beneath North Central Arabia. Proceedings of the International Kimberlite Conference, p. 434.
Torfstein, A., Hammerschmidt, K., Friedrichsen, H., Starinsky, A., Garfunkel, Z., Kolodny, Y., 2013. Helium isotopes in Dead Sea Transform waters. Chemical Geology 352, 188–201.
Trull, T., Kurz, M., 1993. Experimental measurements of ^{3}He and ^{4}He mobility in olivine and clinopyroxene at magmatic temperatures. Geochimica et Cosmochimica Acta 57, 1313–1324.
Vance, D., Stone, J., O'Nions, R., 1989. He, Sr and Nd isotopes in xenoliths from Hawaii and other oceanic islands. Earth and Planetary Science Letters 96, 147–160.
Wallace, M.E., Green, D.H., 1988. An experimental determination of primary carbonatite magma composition. Nature 335, 343–346.
Wang, H., van Hunen, J., Pearson, D.G., 2015. The thinning of subcontinental lithosphere: the roles of plume impact and metasomatic weakening. Geochemistry, Geophysics, Geosystems 16 (4), 1156–1171.
Wass, S.Y., Rogers, N., 1980. Mantle metasomatism—precursor to continental alkaline volcanism. Geochimica et Cosmochimica Acta 44, 1811–1823.